The Astronomical Journal, 165:197 (29pp), 2023 May https://doi.org/10.3847/1538-3881/acc4c6

Catching Tidal Dwarf Galaxies at a Later Evolutionary Stage with ALFALFA

Laurin M. Gray[1], Katherine L. Rhode[1], Lukas Leisman[2], Pavel E. Mancera Piña[3], John M. Cannon[4], John J. Salzer[1], Lexi Gault[1], Jackson Fuson[4], Gyula I. G. Józsa[5,6], Elizabeth A. K. Adams[7,8], Nicholas J. Smith[1], Martha P. Haynes[9], Steven Janowiecki[10], and Hannah J. Pagel[1]
[1] Department of Astronomy, Indiana University, 727 East Third Street, Bloomington, IN 47405, USA; grayla@iu.edu
[2] Department of Astronomy, University of Illinois, 1002 W. Green Street, Urbana, IL 61801, USA
[3] Leiden Observatory, Leiden University, P.O. Box 9513, 2300 RA Leiden, The Netherlands
[4] Department of Physics & Astronomy, Macalester College, 1600 Grand Avenue, Saint Paul, MN 55105, USA
[5] Max-Planck-Institut für Radioastronomie, Auf dem Hügel 69, D-53121 Bonn, Germany
[6] Department of Physics and Electronics, Rhodes University, PO Box 94, Makhanda, 6140, South Africa
[7] ASTRON, Netherlands Institute for Radio Astronomy, Oude Hoogeveensedijk 4, 7991 PD Dwingeloo, The Netherlands
[8] Kapteyn Astronomical Institute, Landleven 12, 9747 AD Groningen, The Netherlands
[9] Cornell Center for Astrophysics and Planetary Science, Space Sciences Building, Cornell University, Ithaca, NY 14853, USA
[10] University of Texas, Hobby-Eberly Telescope, McDonald Observatory, TX 79734, USA
Received 2022 August 3; revised 2023 March 9; accepted 2023 March 13; published 2023 April 13

Abstract

We present deep optical imaging and photometry of four objects classified as "Almost-Dark" galaxies in the Arecibo Legacy Fast Arecibo L-band Feed Array (ALFALFA) survey because of their gas-rich nature and extremely faint or missing optical emission in existing catalogs. They have H I masses of 10^7–10^9 $M_\odot$ and distances of ∼9–100 Mpc. Observations with the WIYN 3.5 m telescope and One Degree Imager reveal faint stellar components with central surface brightnesses of ∼24–25 mag arcsec^{-2} in the g band. We also present the results of H I synthesis observations with the Westerbork Synthesis Radio Telescope. These Almost-Dark galaxies have been identified as possible tidal dwarf galaxies (TDGs) based on their proximity to one or more massive galaxies. We demonstrate that AGC 229398 and AGC 333576 likely have the low dark matter content and large effective radii representative of TDGs. They are located much farther from their progenitors than previously studied TDGs, suggesting they are older and more evolved. AGC 219369 is likely dark matter dominated, while AGC 123216 has a dark matter content that is unusually high for a TDG, but low for a normal dwarf galaxy. We consider possible mechanisms for the formation of the TDG candidates such as a traditional major merger scenario and gas ejection from a high-velocity flyby. Blind H I surveys like ALFALFA enable the detection of gas-rich, optically faint TDGs that can be overlooked in other surveys, thereby providing a more complete census of the low-mass galaxy population and an opportunity to study TDGs at a more advanced stage of their life cycle.

Unified Astronomy Thesaurus concepts: Dwarf irregular galaxies (417); Galaxy evolution (594); Galaxy interactions (600); Galaxy photometry (611)

1. Introduction

The Arecibo Legacy Fast Arecibo L-band Feed Array (ALFALFA) blind extragalactic H I survey (Giovanelli et al. 2005; Haynes et al. 2018) was designed primarily to probe the low-mass end of the H I mass function and has identified over 31,000 sources out to a redshift z ∼0.06. ALFALFA covered nearly 7000 square degrees of sky and detected H I sources without regard for their optical properties, which makes it a powerful tool to search for tidal remnants such as tidal dwarf galaxies (TDGs) on a larger scope than previously attempted (Giovanelli et al. 2005).

TDGs are generally composed of material removed from a parent galaxy through tidal interactions, which means they are usually very gas-rich (Duc 2012). They have masses and sizes comparable to dwarf galaxies and over time will become dynamically stable systems independent of their parent galaxy (Duc 2012). TDGs contain clues to the interaction histories of their parent galaxies, potentially constraining the interaction type and properties of the merging systems (Lee-Waddell et al. 2014). They are also vital for determining cosmological constraints in group environments (Lee-Waddell et al. 2014).

TDGs usually have higher metallicities than normal dwarf galaxies because they are created out of preenriched material stripped from the outer disks of larger galaxies (Duc 1999; Duc et al. 2000; Weilbacher et al. 2000; Duc 2012). However, Hunter et al. (2000) point out that very old tidal dwarfs, which were formed before spirals could become more enriched, could have metallicities similar to modern metal-poor dwarfs. TDGs have a very low dark matter content, because tidal forces create gas-rich streams that contain a small fraction of preexisting stars and almost no dark matter, and the potential gravitational well of the dwarf is too shallow to capture dark matter (Bournaud 2010). The turbulence of the tidal interaction also frequently triggers star formation, leading to a population of young blue stars (Duc et al. 2000).

Kaviraj et al. (2012) conducted a statistical survey of the properties of 405 optically identified TDG candidates and their parent systems and found that the vast majority of TDGs are within 20 kpc of their progenitors. However, the most easily identified TDG candidates still have a visible tidal tail connecting them to their parents. As a result, the sample of known TDGs is biased toward objects that are near their parent galaxies and still in the early stages of their evolution, as the tail

takes time to dissolve. Simulations suggest that to become a bona fide TDG, a tidal knot must have enough mass ($\geqslant 10^8\ M_\odot$) and distance from the gravitational well of the parent to become self-gravitating and avoid falling back into the parent system (Bournaud & Duc 2006). Therefore, the overall sample of objects that have been studied consists mainly of TDG candidates, with some uncertainty as to whether they will become long-lived (>1 Gyr; Bournaud & Duc 2006; Kaviraj et al. 2012). It is also uncertain how long TDGs are able to remain stable without a massive dark matter halo, as simulations indicate that dark-matter-deficient, rotationally supported galaxy disks are prone to axisymmetric and nonaxisymmetric instabilities on dynamical timescales (Sellwood & Sanders 2022). As TDGs evolve, they become optically indistinct from other satellite dwarf galaxies (Duc 2012). Identification relies on metallicity measurements and age estimations, usually from time-intensive spectroscopy. Additionally, the initial burst of star formation will eventually end, the young stellar population will age, and the higher metallicity will contribute to a faster rate of dimming, making older TDGs even more difficult to detect through optical methods (Román et al. 2021). However, they will remain gas-rich, so H I observations are useful for locating objects of interest when searching for TDGs because they will be able to catch sources with extremely low optical surface brightnesses.

Around 99% of the objects observed in ALFALFA could be matched to objects in previously published optical catalogs such as the Sloan Digital Sky Survey (SDSS; Eisenstein et al. 2011), though many had never been observed in H I before. The remaining 1% is a set of gas-rich objects that are missing a clear counterpart in optical catalogs. A subset of these are classified as Ultra-Compact High-Velocity Clouds (UCHVCs; Giovanelli et al. 2010; Adams et al. 2013), which are compact H I clouds with velocities consistent with a location in the vicinity of the Local Group. Follow-up optical imaging of the UCHVCs has in some cases revealed a dwarf galaxy or other possible stellar counterpart (see Rhode et al. 2013; Sand et al. 2015; Janesh et al. 2019). The remaining objects without clear optical counterparts are classified as "Almost-Dark" galaxies (ADs); these objects have velocities that place them outside of the Local Group and H I masses ranging from 10^7 to $10^9\ M_\odot$. Deep optical imaging of several ADs has revealed low-surface-brightness stellar components that were below the sensitivity limits of previous surveys (Cannon et al. 2015; Leisman et al. 2021). As explained in Cannon et al. (2015), while the majority were either OH megamasers or tidal debris from a nearby galaxy interaction, a small subset appeared to be more isolated. Some of the ADs have properties that make them comparable to ultradiffuse galaxies (UDGs; van Dokkum et al. 2015; Leisman et al. 2017; Gault et al. 2021). Other ADs have been identified as likely TDGs that have moved farther away from their parent sources than the majority of previously studied TDGs (Lee-Waddell et al. 2016). As we will discuss in this paper, TDGs (particularly evolved TDGs) have low central surface brightnesses and large effective radii, which means that some TDGs may fit the criteria used to define UDGs, so there may be overlap between the two categories.

In this paper, we present H I and optical data of four objects that have been classified as potential Almost-Dark TDGs (AD-TDGs). The four objects, AGC 123216, AGC 219369, AGC 229398, and AGC 333576, were selected from the AD sample and identified as potential TDGs because of the presence of at least one H I-rich source that could be classified as a potential parent galaxy based on that galaxy's proximity and velocity relative to the AD. In particular, the potential parent galaxies for each AD-TDG candidate are located within 500 kpc on the sky at the reported distance for the AD and have a measured heliocentric velocity that is within ± 500 km s^{-1} of the AD as measured by Haynes et al. (2011). The four AD-TDG candidates we analyzed each have between one and three potential parent galaxies meeting these criteria.

The paper is organized as follows. Section 2 covers the H I and optical observations and data processing. Section 3 describes the procedures used to carry out our measurements of quantities such as optical surface brightness, and stellar, baryonic, and dynamical masses. A discussion of the properties and environment of each AD is given in Section 4. Section 5 discusses the ADs in the context of our current understanding of TDGs, including comments on their possible origins. The last section includes a brief summary of our main conclusions.

2. Observations and Data Processing

2.1. H I Data

The AD ALFALFA observations and data reduction processes are described in detail in other papers (Giovanelli et al. 2005; Saintonge 2007; Haynes et al. 2011), and the relevant ALFALFA catalog (Haynes et al. 2018) measurements for these objects and their possible parents are reproduced in Table 1, along with photometric data from SDSS for the possible parents for reference (Ahumada et al. 2020). Generally, the distance for objects with $v_{\rm helio} > 6000$ km s^{-1} was estimated with the Hubble Law (with $H_0 = 70$ km s^{-1} Mpc^{-1}), and the local peculiar velocity model of Masters (2005) was used for distances of objects with $v_{\rm helio} < 6000$ km s^{-1}.

In addition to the original ALFALFA observations, the ADs presented in this paper and their prospective progenitors were also observed with the Westerbork Synthesis Radio Telescope (WSRT) in an exploratory observational program of a larger subset of Almost-Dark galaxies (program R13B/001; PI Adams). Observations consisted of two 12 hour pointings centered on the central H I velocity from ALFALFA, using a 10 MHz bandpass with 1024 channels and two polarizations. Data reduction is detailed in Janowiecki et al. (2015) and Leisman et al. (2016). The reduction used an automated pipeline based on the MIRIAD (Sault et al. 1995) data software (see Serra et al. 2012; Wang et al. 2013). The pipeline automates radio frequency interference flagging and implements primary bandpass calibration, and iterative deconvolution of the data with the CLEAN algorithm to apply self-calibration. We used a robustness weighting $r = 0.4$ and a velocity resolution binning of 6.0 km s^{-1} after Hanning smoothing. The resulting images had synthesized beams with major (north–south) axes ranging from 32″ to 38″ and minor axes from 13″ to 17″. We also performed primary-beam correction to our measured column densities; note that the FWHM of the WSRT primary beam is ∼35′ at 1.4 GHz, so the column density sensitivity for potential parent sources near the edges of our images is low. Total intensity and velocity field maps were created as detailed in Gault et al. (2021). We were able to retrieve the peak H I column density from the total intensity maps, under the assumption that the flux is spread out over the beam, so this measurement is dependent on the resolution of the beam. The peak H I column density is reported in the Results section for each source.

Table 1
H I Measurements and Other Properties of Candidate AD-TDGs and Potential Parent Galaxies

ID	Classification	R.A. (deg)	Decl. (deg)	v_{helio} (km s^{-1})	W20 (km s^{-1})	Distance (Mpc)	Angular Separation (kpc)	log($M_{H\,I}$)	g (mag)	g–r (mag)
AGC 123216	Almost-Dark	31.17792	28.80583	5111 ± 14	51 ± 7	70.5 ± 2.3	⋯	8.65 ± 0.08	⋯	⋯
MRK 365[a]	Spiral	31.07729	28.65592	5151 ± 5	⋯	72.2 ± 5.1	214 ± 7	⋯	14.33	0.67
NGC 807	Elliptical[b]	31.22917	28.98889	4750 ± 218	492 ± 12	67.7 ± 4.4	231 ± 8	9.79 ± 0.07	14.20	0.87
MCG 05-06-003	Spiral	31.38208	28.61083	5312 ± 92	202 ± 5	73.4 ± 2.3	331 ± 11	9.7 ± 0.05	14.47	0.39
AGC 219369[c]	Almost-Dark	165.96333	28.68583	667 ± 11	45 ± 7	9.2 ± 2.2	⋯	7.25 ± 0.21	⋯	⋯
NGC 3510	Spiral	165.93668	28.88806	704 ± 92	199 ± 2	16.7 ± 3.3	33 ± 8	9.45 ± 0.18	13.33	0.28
AGC 229398	Almost-Dark	180.16251	21.41556	6965 ± 14	49 ± 3	104 ± 2.3	⋯	9.28 ± 0.05	⋯	⋯
KUG 1158+216	Spiral	180.16458	21.3525	7388 ± 125	268 ± 42	110.1 ± 2.3	102 ± 2	9.47 ± 0.06	16.36	0.59
UGC 6989	Spiral	180.02415	21.64528	6404 ± 99	220 ± 3	96 ± 2.4	482 ± 11	9.87 ± 0.05	15.80	0.38
AGC 333576	Almost-Dark	358.185	28.74667	7031 ± 13	37 ± 3	93.9 ± 4.3	⋯	9.1 ± 0.07	⋯	⋯
NGC 7775	Spiral	358.09833	28.77083	6760 ± 65	182 ± 8	93.9 ± 4.3	127 ± 6	9.88 ± 0.06	13.74	0.54

Notes. The data are taken from Haynes et al. (2018) except when otherwise noted. Almost-Dark galaxies are listed at the top of each subsection and followed by their potential progenitors. The classification for the potential parent galaxies is the galaxy type listed on the NASA/IPAC Extragalactic Database (NED; NASA/IPAC Extragalactic Database (NED) 2019). R.A. and decl. are the coordinates for the center of the H I source from ALFALFA, which is not necessarily the center of the optical component. The angular separation in kiloparsec is calculated at the ALFALFA distance of the relevant AD. Listed magnitudes are the CModelMags from SDSS DR16 (Ahumada et al. 2020), corrected for extinction using the Schlegel et al. (1998) extinction maps.

[a] MRK 365 is not included in the ALFALFA catalog, so the distance listed here is the NED Hubble flow distance for the heliocentric velocity measured by Thuan et al. (1999), corrected for a 3K CMB according to Fixsen et al. (1996).

[b] See discussion of classification for NGC 807 in Section 4.1.

[c] The H I mass and angular separation in kpc were calculated using the Haynes et al. (2018) distance of 9.2 Mpc, see Section 4.2 for a discussion on the ambiguity in this measurement.

2.2. Optical Data

Optical observations of the ADs and their surrounding areas were carried out with the WIYN 3.5 m telescope. One object (AGC 229398) was observed in March 2014 with the One Degree Imager with a partially populated focal plane (pODI). Before a larger detector array was installed in 2015, pODI had a 3×3 grid of orthogonal transfer arrays (OTAs), with a field of view of $24'' \times 24''$. There were also four more OTAs in the outer corners that were used to image guide stars. Each OTA is an 8×8 arrangement of 480×496 pixel CCDs, where each pixel has a pixel scale of $0\farcs11$ pixel^{-1}. The other three objects were observed on multiple occasions between 2017 and 2019 with the One Degree Imager (ODI; Harbeck et al. 2014). The ODI camera has 17 additional OTAs compared to pODI, arranged in a 5×6 grid for a field of view of $40' \times 48'$. During each observing run, each source was observed in the g' and r' bands, using a nine-point dither pattern of 300 s per exposure to avoid gaps in the final image resulting from gaps in the CCD array.

We reduced our observations using the One Degree Imager Pipeline, Portal, and Archive (ODI-PPA; Gopu et al. 2014) QuickReduce (Kotulla 2014) data reduction pipeline. The pipeline consists of the following: saturated pixel masking; corrections for crosstalk, persistence, and nonlinearity; overscan subtraction; bias, dark, and flat-field corrections; pupil ghost corrections; and cosmic-ray removal. We then stacked our images using the SWarp program (Bertin et al. 2002) integrated with ODI-PPA's Stack interface. Due to the faintness of these objects, we created the deepest combined images possible without sacrificing image quality by using the best exposure at each dither point and then including any additional exposures with good focus and seeing below $1\farcs5$. The total integration times of the images vary from 45 to 90 minutes based on the number of exposures included in the stack. The background of each image was mapped and subtracted, and then the images were resampled, combined with a weighted average, and reprojected to a pixel scale of $0\farcs125$ pixel^{-1}. An average background value was then added back to each image. The average FWHM values of the point-spread function (PSF) in the stacked images ranges from $0\farcs8$ to $1\farcs1$ in g', and $0\farcs6$ to $1\farcs0$ in r'.

3. Data Analysis and Measurement Procedures

3.1. Gas Mass

In this paper, we make use of two measurements of the H I mass, which are derived independently from the ALFALFA observations and the WSRT observations. Measurements derived from the ALFALFA H I measurements are denoted with a prime ($'$). The ALFALFA H I mass was taken from Haynes et al. (2018), which calculated it as a function of the flux S'_{21} and the distance D' in Mpc using

$$M'_{\rm HI}[M_\odot] = 2.356 \times 10^5 D'^2 S'_{21}, \quad (1)$$

with an uncertainty calculated with

$$\sigma_{log M'_{\rm HI}} = \frac{\sqrt{\left(\frac{\sigma_{S'_{21}}}{S'_{21}}\right)^2 + \left(\frac{2\sigma_{D'}}{D'}\right)^2 + 0.1^2}}{ln(10)}. \quad (2)$$

The WSRT H I mass $M_{H\,I}$ and its associated uncertainty were calculated using the WSRT data with the same equations. In three of four cases, the masses yielded by both measurements were in agreement within uncertainties, but for AGC 229398, WSRT appears to have only recovered about 40% of the mass measured by ALFALFA.

The mass of atomic gas in an AD was estimated by multiplying the H I mass by 1.33 in order to account for the presence of helium. Molecular gas is not expected to be a significant contributor to mass in ADs; Wang et al. (2020) suggest that the main contributor to the low star formation rate of ADs is a low efficiency of conversion of atomic gas to molecular gas. The measurements of atomic and molecular gas in TDGs in Lelli et al. (2015) indicate that the molecular gas mass can range from a few percent up to about a third of the atomic gas mass, though these estimates are for young objects which presumably have a larger reservoir of H_2 gas to support their higher current star formation rate compared to the AD-TDG candidates. As we were not sure which (if any) of these objects are TDGs, we did not want to overestimate the gas or baryonic content; therefore, the baryonic mass calculation did not consider molecular gas as a significant contributor, and so $M'_{\rm atomic} = 1.33 \times M'_{\rm HI} = M'_{\rm gas}$ for data originating from ALFALFA and $M_{\rm atomic} = 1.33 \times M_{\rm HI} = M_{\rm gas}$ for WSRT data.

3.2. H I Kinematics

The H I observations of our galaxies allow us to explore their kinematics and investigate whether the systems show signs of rotational support or if their interstellar medium is more dominated by turbulence. TDGs are expected to be primarily supported by rotation (e.g., Duc et al. 2007; Duc 2012; Lelli et al. 2015), but measuring rotation in TDGs is challenging, especially for lower-mass objects (Hibbard et al. 2001; Lee-Waddell et al. 2012; Duc et al. 2014; Lee-Waddell et al. 2014). Figure 1 shows the WSRT moment one maps for each AD and its potential parent galaxies, as well as a close-up of the velocity field for each AD, with WSRT H I column density contours overlaid. The distortions in the H I maps themselves will be discussed in the results sections for each object. In the early stages of a TDG's evolution, we would expect a continuity in the velocity gradient between a parent and the TDG along the tidal tail connecting them. However, this link will diminish over time as the tail fades, the parent system restabilizes, and the TDG moves away. Because of this, while the presence of such a connection would support identification of a TDG, the absence of one does not disqualify it. From the left panels of Figure 1, there do not appear to be any H I tails connecting an AD to a potential parent galaxy. AGC 219369 appears to be close to the velocity at the southern end of NGC 3510 and the velocity of AGC 333576 follows the direction of the gradient that is across NGC 7775, but otherwise there are no obvious relationships in velocity–space between the AD-TDG candidates and any of their potential parents. The velocity fields of the ADs themselves appear to be messy and disordered, with the exception of AGC 123216 which appears to show some ordered rotation.

Given the low spatial resolution of the WSRT observations, extracting kinematic information is not straightforward as the observations are heavily affected by beam smearing, which tends to erase velocity gradients and to increase the apparent gas velocity dispersion (Swaters 1999; Józsa et al. 2007; Di Teodoro & Fraternali 2015). In order to account for this when extracting kinematic information from our data, we use the software ^{3D}Barolo (Di Teodoro & Fraternali 2015), which incorporates a forward-modeling approach that considers the beam shape of our observations, and therefore is largely unaffected by beam smearing (Józsa et al. 2007; Di Teodoro & Fraternali 2015; Iorio et al. 2017; Mancera Piña et al. 2020).

Prior to running ^{3D}Barolo, we obtain independent constraints on the geometrical parameters (center, kinematic position angle, and inclination). The inclination, i, is a particularly crucial parameter given that $V_{\rm rot} = V_{l.o.s}/\sin(i)$. While ^{3D}Barolo can constrain the inclination angle at high spatial resolution, this becomes challenging for low-resolution observations (and for slowly rising rotation curves in general), and therefore we estimate the geometric parameters based only on the H I morphology of the galaxies and independently from the kinematics. The approach we follow has already been introduced in Mancera Piña et al. (2020), Fraternali et al. (2021), and Mancera Piña et al. (2022b), and consists of generating a set of beam-convolved, azimuthally averaged models of our galaxies with different geometrical parameters drawn from flat prior distributions using a Markov Chain Monte Carlo (MCMC) Bayesian framework.[11] Each model is compared against the real total intensity map, and residuals are minimized using a χ^2 routine. Given that the inclination can have a degeneracy with the thickness of the disks, which we do not know precisely for our galaxies, we performed different tests assuming razor-thin and thick disks up to about 500 pc motivated by observations (Bacchini et al. 2020; Mancera Piña et al. 2022a), finding a very good agreement between both methods. We use our MCMC method to estimate the center, position angle, and inclination of our galaxies based on their H I morphology, and we fix those parameters when modeling the data with ^{3D}Barolo.

We show our kinematic models in Figure 2, where we display the major-axis position–velocity slices of the data and best-fitting model. For these models, we have used a ring separation of length $\sqrt{b_{\rm maj} \times b_{\rm min}}$. AGC 123216, AGC 219369, and AGC 333576 show clear gradients in velocity, although the gas velocity dispersion is of comparable magnitude. The results of the modeling indicate that the velocity gradients can be attributed to a disk with differential rotation for these three galaxies. For AGC 229398, we did not manage to obtain a fully satisfactory model, but our preliminary results indicate that the system may be pressure supported. More definitive models would require data with a much higher angular resolution.

For completeness, we include the emission-line channel maps of each of our galaxies and their best-fitting models in Appendix With each channel showing the line-of-sight velocities around the systemic velocity, the maps show evidence for rotation in AGC 123216, AGC 219369, and AGC 333576.

3.3. Dynamical Mass

For a self-gravitating object, the dynamical mass of the H I region within the radius $r_{\rm H\,I}$ can be estimated as

$$M_{\rm dyn}[M_\odot] = 6.78 \times 10^4 r_{\rm HI} D' \left(\frac{W'_{20}}{2\sin(i)} \right)^2, \quad (3)$$

where $r_{\rm H\,I}$ is the radius of the H I in arcminutes derived from the kinematic modeling, D' and W'_{20} are the distance to the source in Mpc and the width of the velocity profile at 20% of the peak flux density in km s^{-1}, respectively (Haynes et al. 2018). The inclination i is derived from the MCMC fitting of geometric parameters described in Section 3.2.

[11] The software to do this is called Cannubi, and it is available at https://www.filippofraternali.com/cannubi.

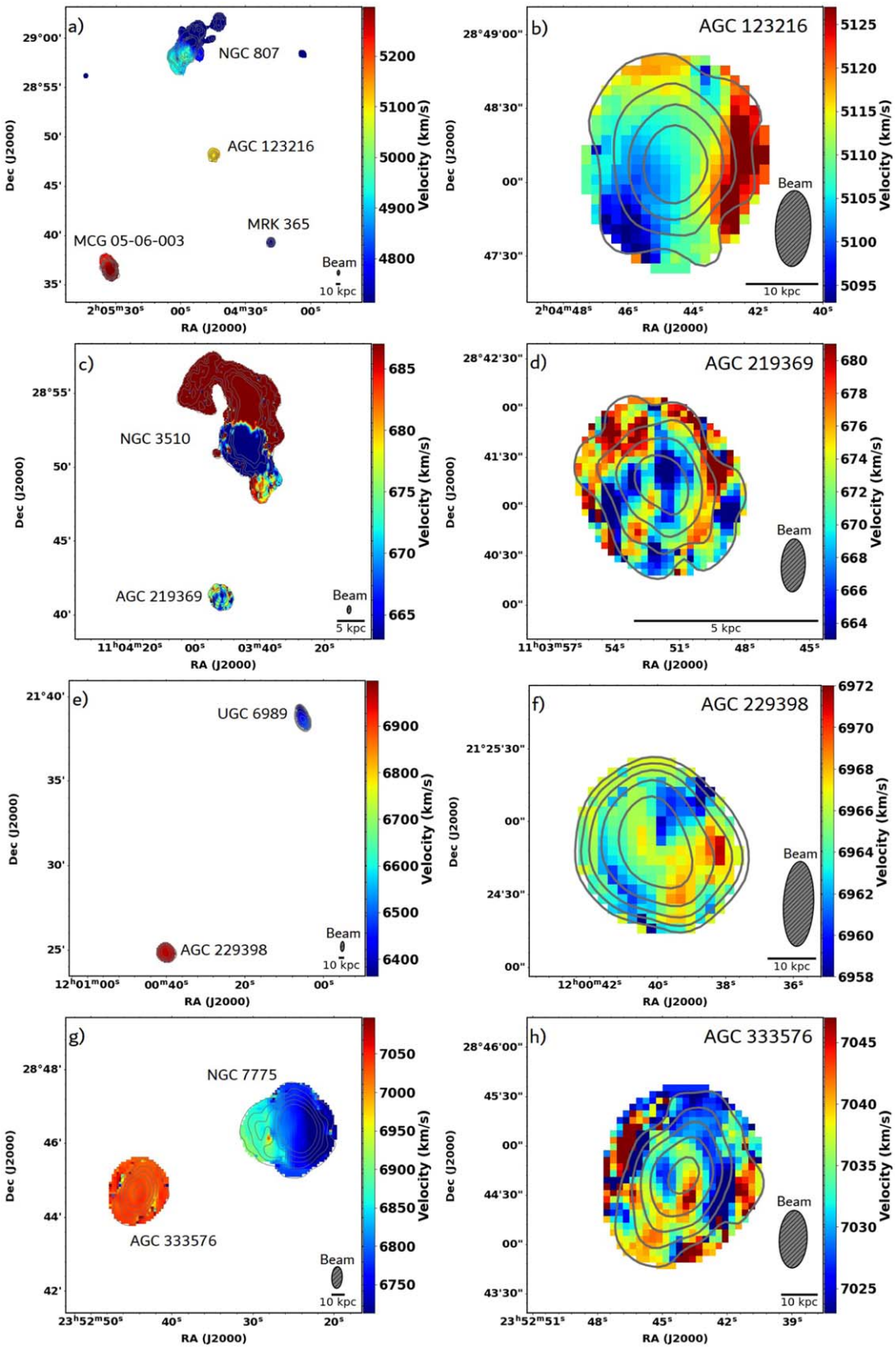

Figure 1. Moment one velocity maps from WSRT imaging, with WSRT H I column density contours superimposed in dark gray, for (from top to bottom) AGC 123216, AGC 219369, AGC 229398, and AGC 333576, and their nearby potential parent galaxies. The left panels show the full field around each AD, and the right panels show a close-up of the AD. Beam size is shown as a shaded gray ellipse. The figures for AGC 123216, AGC 219369, and AGC 333576 have column density contours at $N_{\rm H\,I} = (0.1, 0.5, 1.2, 2.4, 4.5) \times 10^{20}$ cm^{-2}, while the figures for AGC 229398 have contours at $N_{\rm H\,I} = (0.1, 0.2, 0.4, 0.8, 1.6) \times 10^{20}$ cm^{-2}, where the lowest contours are the first listed. Note that KUG 1158+216 is not included in the full-field map for AGC 229398 because we did not have WSRT H I maps for it.

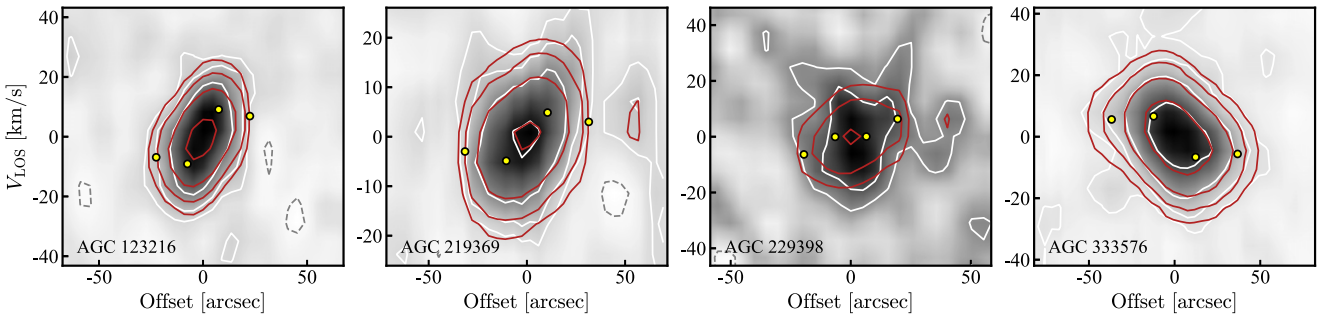

Figure 2. Position–velocity slices of 1 pixel width along the major-axis from the best-fitting model of each AD-TDG candidate, from WSRT data. The data are shown in gray, with white contours at 2, 4, 8, and 16 times the S/N of the data. Dashed dark gray contours represent $-2 \times$ S/N. The red contours represent the best-fit model, and the yellow points mark the line-of-sight rotation velocities from the model.

TDGs are distinguished by their low dark matter content, which we evaluate using the dynamical-to-gas mass ratio, so we want to ensure that we are not underestimating the dynamical mass. Due to the relatively narrow line widths of the H I for these objects, we used W'_{20} rather than the more commonly used width at 50% of the velocity profile peak W'_{50}, which will provide a more stringent upper limit on the dynamical mass. Additionally, using the emission-line width as a proxy for the rotation velocity overestimates the dynamical mass due to artificial line broadening from beam-smearing effects (Lelli et al. 2015). This effect is more pronounced in systems where the velocity dispersion is of comparable magnitude to the rotational velocity (Lelli et al. 2015), which is the case for these objects. However, it is also important to consider that if the ADs are more pressure supported than rotation supported, these dynamical mass values may be comparatively underestimated. These measurements do not account for turbulence and asymmetric drift, which may also increase the dynamical mass estimate. We estimated a rough correction for turbulence and asymmetric drift using

$$M_{\rm dyn}[M_\odot] = 6.78 \times 10^4 r_{\rm HI} D' \left(\left(\frac{\sqrt{W'^2_{20} - \sigma^2}}{2\sin(i)} \right)^2 + 3\sigma^2 \right), \quad (4)$$

and a velocity dispersion (σ) of 11 km s^{-1} to evaluate how it may affect the results. We found that it increased the dynamical mass calculated by 23% for AGC 123216, 40% for AGC 219369, 45% for AGC 229398, and 66% for AGC 333576. However, this did not change the conclusions about the nature of each object (see Section 5.6), and so the reported values do not reflect this correction as it was mostly exploratory. As stated previously, a robust estimation of the correction through kinematic modeling would require data with a much higher spatial resolution (Iorio et al. 2017).

This calculation assumes that the sources are in dynamical equilibrium, which is a reasonable assumption given the distances of the objects from any nearby perturbers. The apparent rounded shapes of the H I distributions may be an additional indicator of dynamical equilibrium, but this may also be an effect of the elongated beam of WSRT, which could be artificially extending the emission along that axis. Both the MCMC routine and ^{3D}Barolo take this beam smearing into account for the geometric fitting and kinematic modeling.

3.4. Photometry and Surface Brightness

We measured surface brightness profiles for the AD-TDG candidates using a procedure similar to those described in Mancera Piña et al. (2019) and Marasco et al. (2019). Briefly, a concentric set of ellipses were placed, centered on the optical component of the object. The mean pixel brightness and standard deviation within each band (meaning the space between adjacent ellipses) were calculated, and pixels with values more than a certain number of standard deviations above the mean were masked and excluded from further calculations. For AGC 123216, AGC 229398, and AGC 333576, the threshold was five standard deviations, while for AGC 219369 it was four standard deviations. Pixels within three pixels of the one above the threshold were also masked, in order to reduce contamination from an unassociated bright source that may have bled into the surrounding region. A new mean brightness and associated standard deviation were then calculated. The final threshold and mask growth parameters were determined by evaluating the results of various combinations for a setting that was as conservative as possible while still removing objects that were clearly not part of the AD (usually objects that were much brighter, redder, and/or significantly more concentrated). In a few cases, a region was manually masked in order to remain consistent between images (e.g., a very red object that did not have enough emission in the g band to exceed the threshold, but which should still not be included). Due to the faint and irregular nature of the objects, fitting apertures to the objects was done manually. The visible portions of AGC 219369 and AGC 333576 are fairly round, so circular apertures were centered on the optical portion. The optical counterparts of AGC 123216 and AGC 229398 appear to be quite elongated (in spite of their more circular H I gas distributions), so we measured the major and minor axis of the visible components to estimate a center and ellipticity, as well as a position angle. For each of the four sources, ellipses were separated by 2 times the largest FWHM of the two filters for that source. This separation allowed us to achieve a consistent and precise measurement of surface brightness across filters without the space between ellipses being smaller than the resolution scale of the image. Ellipses were extended until the last ellipse before the signal-to-noise ratio (S/N) fell below one in order to be sure we were capturing all of the light. The apparent magnitude was calculated using the total amount of light contained within the outermost ellipse.

We obtained a central surface brightness and effective radius by fitting a Sérsic profile to the observed surface brightness

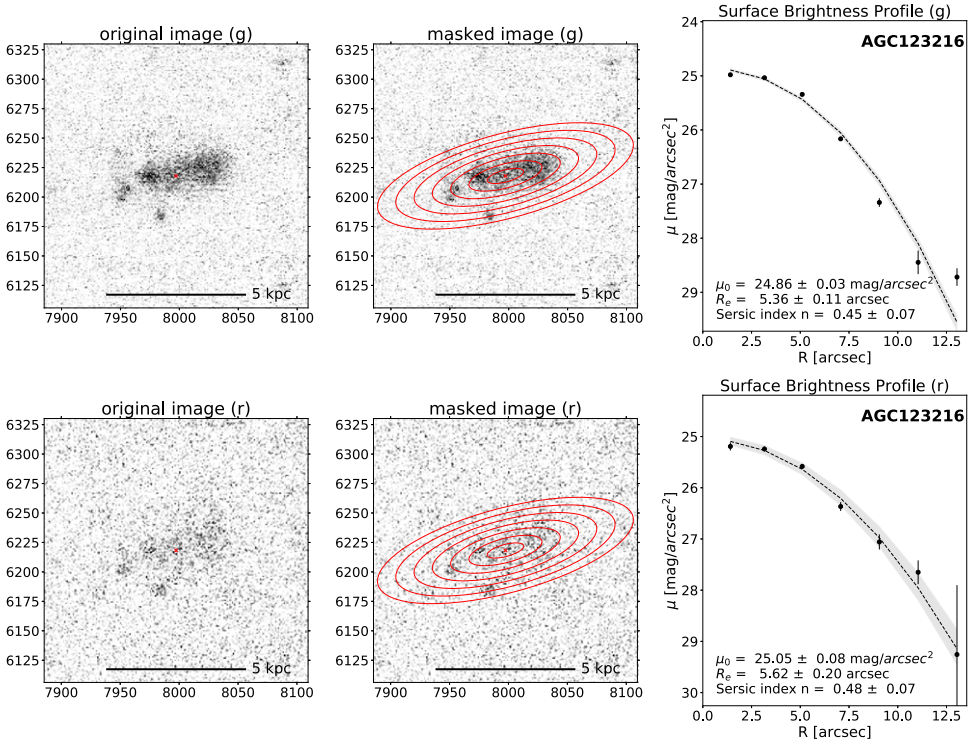

Figure 3. Masking, surface brightness profiles, and profile fit parameters for AGC 123216 in g' (top row of each panel) and r' (bottom row of each panel), with optical images from the WIYN 3.5 m telescope. For each object, the left images show the original image with a small red x marking the optical center; the center images show the ellipses that were placed in red and pixels that were masked in green, based on the masking procedure described in Section 3.4; and the right images show the best-fitting surface brightness profile, along with the uncertainty shaded in light gray and the parameters for that fit listed below. For AGC 123216, there were no pixels flagged for masking in either filter.

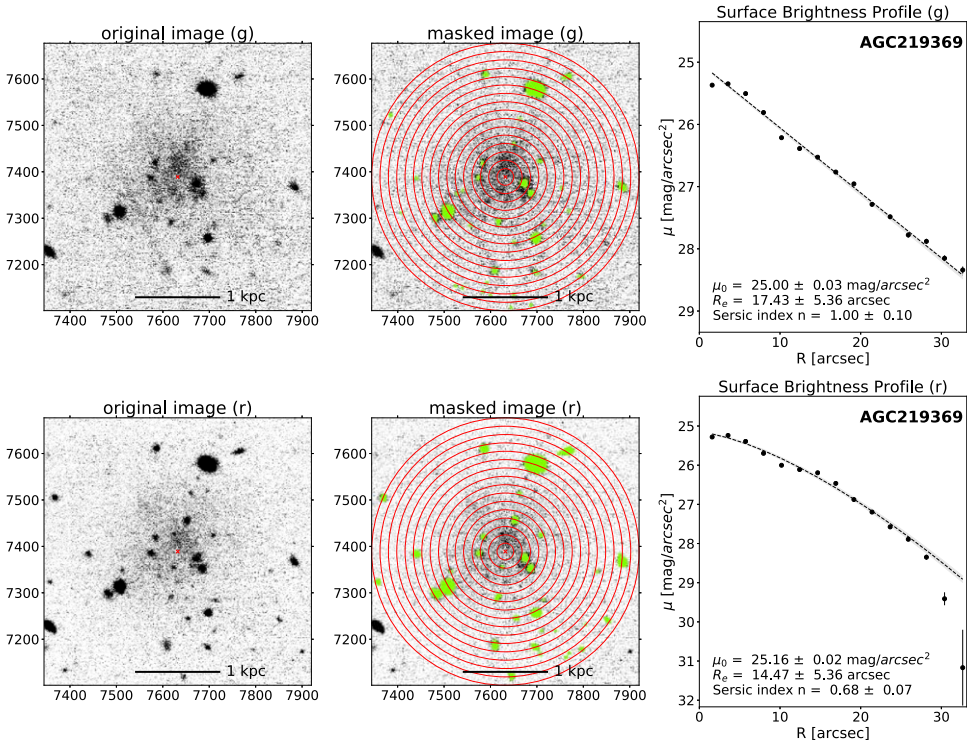

Figure 4. Masking, surface brightness profiles, and profile fit parameters for AGC 219369 in g' (top row of each panel) and r' (bottom row of each panel), with optical images from the WIYN 3.5 m telescope. Figure description is the same as Figure 3. The physical scale bar for AGC 219369 is calculated for a distance of 9.2 Mpc.

profile using the equation

$$\mu(r) = \mu_0 + 1.0857 * b_n^*(r/r_e)^{1/n}, \quad (5)$$

where $\mu(r)$ is the observed surface brightness at radius r, μ_0 is the central surface brightness ($r = 0$), r_e is the effective radius, n is the Sérsic index, and b_n is approximated as

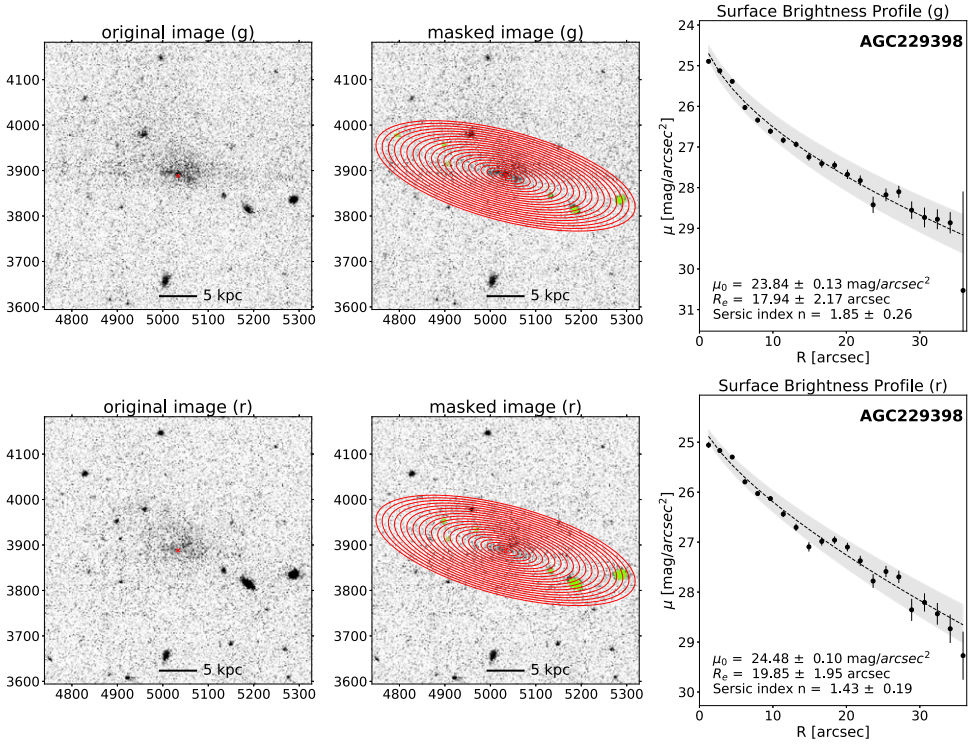

Figure 5. Masking, surface brightness profiles, and profile fit parameters for AGC 229398 in g' (top row of each panel) and r' (bottom row of each panel), with optical images from the WIYN 3.5 m telescope. Figure description is the same as Figure 3.

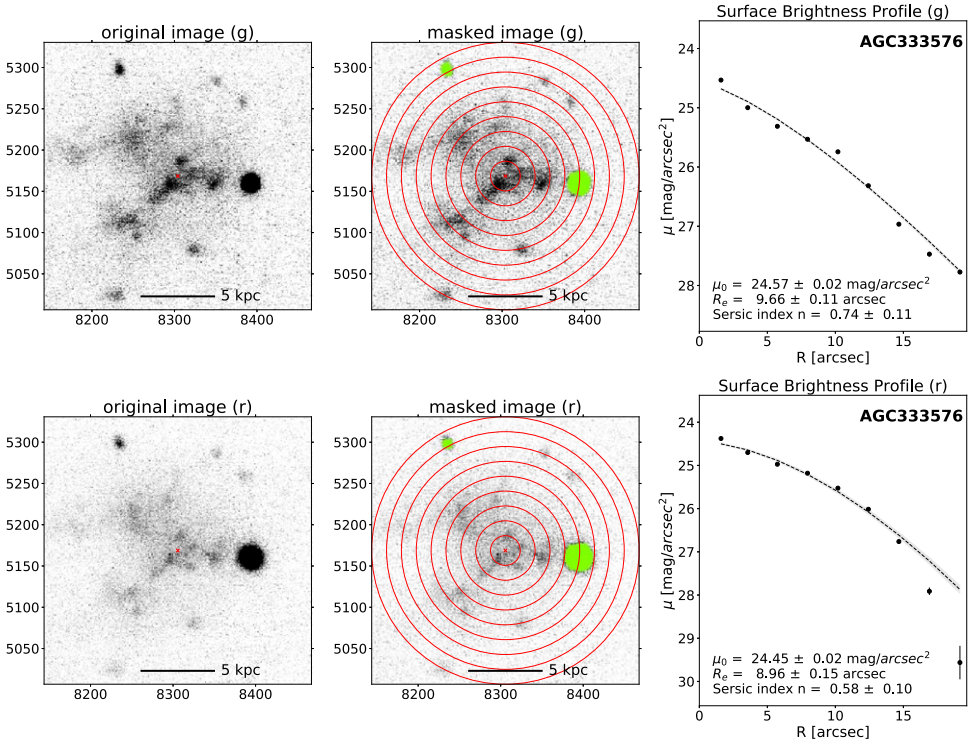

Figure 6. Masking, surface brightness profiles, and profile fit parameters for AGC 333576 in g' (top row of each panel) and r' (bottom row of each panel), with optical images from the WIYN 3.5 m telescope. Figure description is the same as Figure 3.

$2n - \frac{1}{3} + \frac{4}{405n} + \frac{46}{25515n^2} + \frac{131}{1148175n^3} - \frac{2194697}{30690717750n^4}$ for $n > 0.36$ (Ciotti & Bertin 1999). The scale radius r_d was obtained with the relation $r_d = r_e/(b_n)^n$. All of the fits were near-exponential, with n ranging from 0.45 to 1.85. The masking and resulting surface brightness profiles for each AD in g' and r' are shown in Figures 3–6.

We measured the magnitudes and colors of SDSS stars in each field and used them to calculate zero-points and color terms for converting our measured instrumental magnitudes

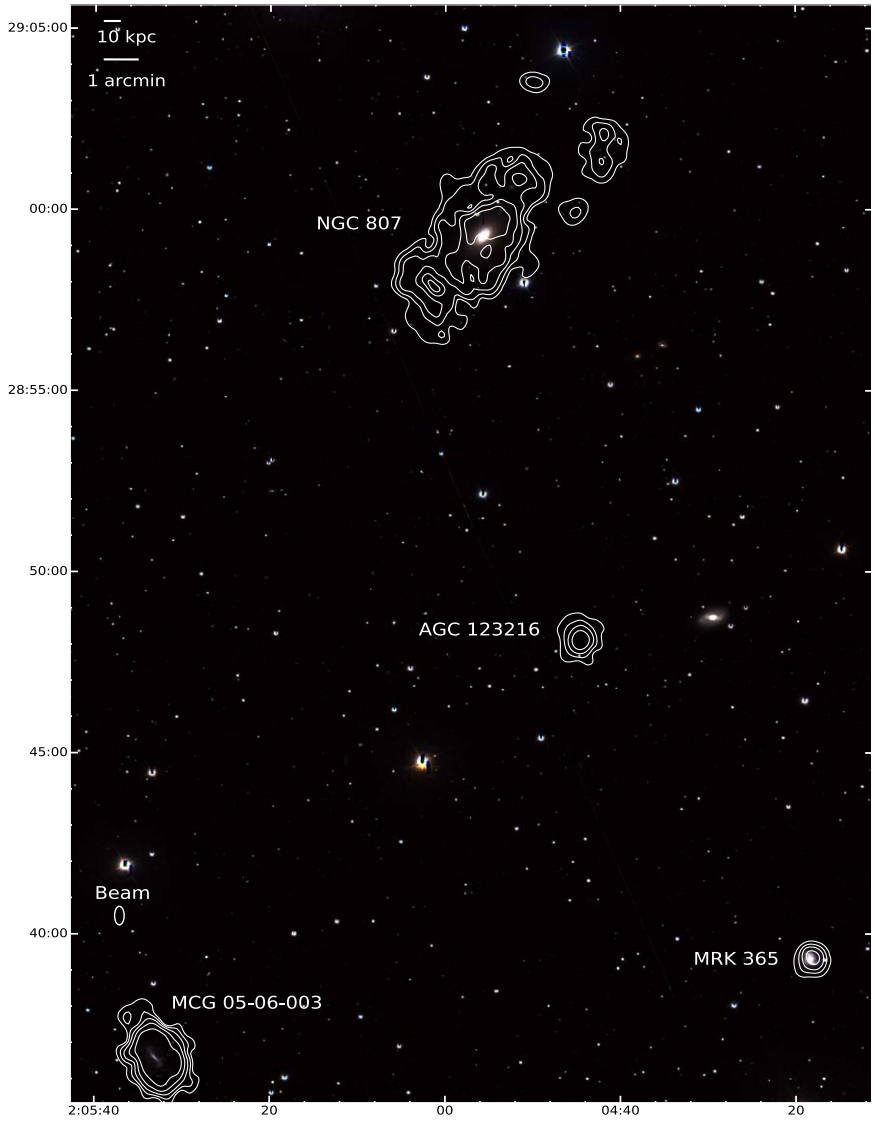

Figure 7. WIYN 3.5 m $g' + r'$-band composite image showing the full-field view of AGC 123216 (center) with potential parents NGC 807 (top), MRK 365 (bottom right), and MCG 05-06-003 (bottom left). There are WSRT H I column density contours at $N_{\rm H\,I} = (0.1, 0.5, 1.2, 2.4, 4.5) \times 10^{20}$ cm^{-2} superimposed in white.

and colors to calibrated values. We also corrected our photometry for extinction using the Schlegel et al. (1998) dust maps and the coefficients from Schlafly & Finkbeiner (2011). Though we report results in both g and r bands, we generally focus on the g-band results, as these objects are quite blue and thus slightly better defined in g. This is made clear by the difference between the leftmost panels of the surface brightness figures for each object, shown in Figures 3–6. Therefore, the effective radius and scale radius reported for each object are those calculated using the g-band image.

3.5. Stellar Mass and Baryonic Mass

We can photometrically estimate the stellar mass ratios and therefore stellar mass of a galaxy using color–stellar mass-to-light ratio relations (CMLRs) that relate the optical color and absolute magnitude to the stellar mass. The CMLRs have been calibrated with model data and observational samples, but the extreme nature of the galaxies in this study means that it is unclear which fits are most appropriate. Using the measured $g - r$ color and total magnitudes from the largest ellipse, we explored the stellar mass-to-light ratio and resulting stellar mass estimates of two CMLRs: Du et al. (2020), which is calibrated for low-surface-brightness galaxies, and Herrmann et al. (2016), which is calibrated for dwarf irregular galaxies. The Herrmann et al. (2016) relation consistently gave the highest stellar masses, and the Du et al. (2020) values are closer in agreement between the two optical bands than the Herrmann et al. (2016) ones. In this paper, we report the average of the values derived in both optical bands between the two relations for the stellar masses of the optical counterparts because it is unclear which is a better fit for this unusual group of objects. The stellar mass uncertainty is heavily dependent on the uncertainty in the color measurement, and was estimated by varying the color by adding or subtracting the associated error and calculating the resulting stellar mass.

We also evaluated the stellar luminosity by using AB solar magnitudes from Willmer (2018) to convert the absolute magnitudes in g and r to luminosity in g and r (L_g and L_r). This allowed us to calculate the H I-mass-to-stellar-luminosity ratios $M'_{\rm HI}/L_g$ and $M'_{\rm HI}/L_r$.

ALFALFA has a larger beam than WSRT, so it is more sensitive to diffuse, low-surface-brightness H I emission and

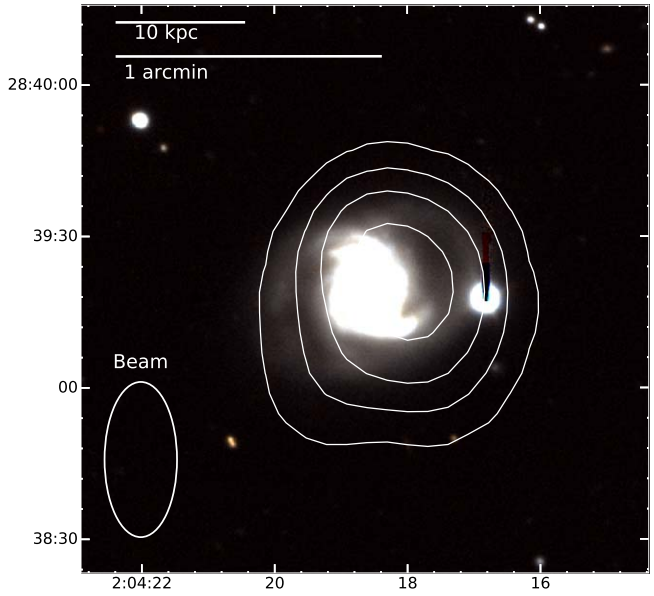

Figure 8. WIYN 3.5 m $g' + r'$-band composite image of MRK 365 with WSRT H I column density contours at $N_{\rm H\,I} = (0.1, 0.5, 1.2, 2.4) \times 10^{20}$ cm^{-2} in white. The H I contours are slightly offset from the stellar disk, and the image is scaled to show a faint loop of stellar emission on the right side, between the first and second innermost contours.

therefore yields a more accurate measurement of the total H I content, so we estimate the baryonic mass as $M'_{\rm bary} = M'_{\rm gas} + M_*$.

4. Results

4.1. AGC 123216

There are three potential parent galaxies within 500 kpc in projected distance and with $v_{\rm helio}$ within 500 km s^{-1} of AGC 123216, all of which show distortions in their H I emission (Figure 7). We discuss them here in order of increasing angular separation from AGC 123216.

MRK 365 is a spiral galaxy to the southwest of AGC 123216. MRK 365 is the potential parent that is closest to AGC 123216, with a minimum projected separation of 214 ± 7 kpc and a heliocentric velocity difference of 40 ± 15 km s^{-1}. The H I gas in MRK 365 appears to be offset from the optical center (Figure 8), and high-sensitivity images reveal a low-surface-brightness string of stellar emission wrapping around the outside of the galaxy. It has been listed in the literature as having a double nucleus, which would suggest a previous or ongoing merger, though there is discussion about whether this is true (Gimeno et al. 2004). Mezcua et al. (2014) constructed a luminosity profile and found that it was consistent with the presence of a single exponential disk; this is a sign that if there is a merger, it is in a late stage.

NGC 807 is the next closest potential parent to AGC 123216, with a minimum projected separation of 231 ± 8 kpc and a heliocentric velocity difference of 361 ± 218 km s^{-1}. It has been classified as an elliptical galaxy in multiple catalogs (Vorontsov-Vel'Yaminov & Arkhipova 1964; Nilson 1973; de Vaucouleurs et al. 1991). As the vast majority of TDGs originate from interactions between gas-rich galaxies, an elliptical galaxy would not normally be considered as a likely progenitor (especially with two other potential spiral parents nearby). However, the extended amount of H I surrounding NGC 807 is unusual for an elliptical galaxy, and it has clearly been disturbed (Figure 7). Figure 1(a) shows two small clumps of H I to the left and right of NGC 807 which appear to have similar heliocentric velocities to that galaxy. The WSRT data are most sensitive toward the center of the image, so due to their location toward the edge of the image, these may not be statistically significant measurements of gas. Additionally, they do not appear as sources in the ALFALFA catalog, which indicates that there is unlikely to be a deposit of low-surface-density gas at these locations that the smaller beam of WSRT is resolving out. Dressel (1987) found that the neutral hydrogen in NGC 807 has the double-horned line profile characteristic of a rotating disk of gas. Further studies with deeper optical imaging have even revealed faint tidal arms (Lucero & Young 2013). Young (2002) mapped the CO emission of NGC 807 and found that it was strongly asymmetric, with 70% of the CO mass being located in the southeast half of the galaxy; Lucero & Young (2013) also estimated that the southeastern tail comprised 70% of the H I gas mass within the tails. Young (2002) mentions that the asymmetry of the CO gas would not be expected to persist for more than 1 Gyr due to shearing by differential rotation. Inspection of Figure 9 reveals that the bright bulge is in the center of a low-surface-brightness spiral disk with dust lanes (left panel), and there are several low-surface-brightness features (tidal arms) extending outward in several directions (right panel). In this way, NGC 807 may have some similarities to UGC 1382, a galaxy believed to be a normal elliptical until deep UV and optical imaging revealed a set of low-surface-brightness spiral arms (Hagen et al. 2016).

At a projected separation of 331 ± 11 kpc, MCG 05-06-003 is the farthest potential parent from AGC 123216. Not much is known about MCG 05-06-003, which appears to be an edge-on spiral galaxy with a significant bar. The H I map shows a slight extension of H I to the northeast, perpendicular to the direction of AGC 123216. Given the closer proximity (see Table 1) along with extensive H I distortion or apparent recent interaction history of the other two potential parent galaxies, we consider MCG 05-06-003 to be the least likely of the three galaxies to be the progenitor of AGC 123216.

AGC 123216 itself has an interesting appearance, with an optical component that is elongated in the east–west direction but surrounded by a relatively rounded concentration of H I gas, although this appearance is somewhat dependent on the elongated beam (Figure 10). The measured properties of AGC 123216 can be found in Table 2, and the surface brightness profiles are shown in Figure 3. It has a central surface brightness in g of 24.86 ± 0.03 mag arcsec^{-2} and an absolute total magnitude in g of -13.44 ± 0.08 mag. The $g - r$ color of -0.11 ± 0.12 makes it exceptionally blue. The effective radius from the Sérsic profile fit is 1.83 ± 0.04 kpc, which combined with the central surface brightness, places it in the regime of UDGs as defined by van Dokkum et al. (2015). The stellar mass of AGC 123216 is estimated at $(3.86 \pm 1.24) \times 10^6$ $M_\odot$, and its H I-to-stellar mass ratio is 115.28 ± 42.20. While it is extremely gas-rich, it has apparently formed relatively few stars for its gas mass. It has a dynamical mass of $(2.33 \pm 0.82) \times 10^9$ $M_\odot$, which yields a dynamical-to-gas mass ratio of 4.40 ± 1.70.

4.2. AGC 219369

AGC 219369 has a heliocentric velocity of 667 ± 11 km s^{-1}, which implies a distance of 9.2 ± 2.2 Mpc according to the Masters (2005) flow model that was used to construct the ALFALFA catalog. However, AGC 219369 is located in the

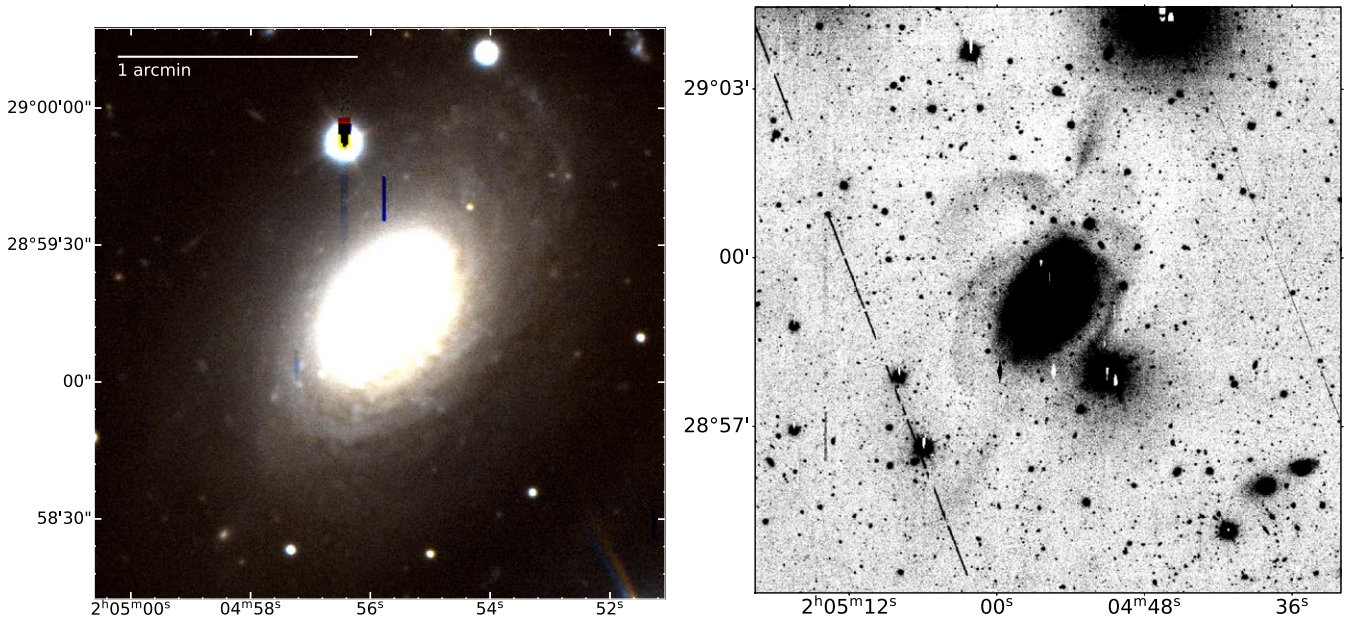

Figure 9. WIYN 3.5 m $g' + r'$-band composite images of NGC 807. Left: Color image revealing low-surface-brightness, dusty spiral arms surrounding a large and bright bulge. The image has been scaled to show the full extent of the faint disk, which overemphasizes the bulge at the center. Right: Composite $g' + r'$-band summed image in inverted grayscale showing arms of stellar emission extending in several directions, primarily out of the northern edge of the disk. The image has been binned 3x3 to make the arms easier to see. Note that this image is a different scale than the left panel, as the region of the disk in that image is the entire black area here.

"triple-value region" of the sky, where proximity to the Virgo Cluster affects the radial velocities of nearby objects such that objects at three different distances can have the same radial velocity (Marinoni et al. 1998; Shaya et al. 2017). This makes measuring the distance to AGC 219369 with only the heliocentric velocity difficult. Redshift-independent Tully–Fisher distance measurements for the nearby spiral galaxy NGC 3510 (which has a similar heliocentric velocity to AGC 219369) place it at 16.8 ± 2.5 Mpc (Tully et al. 2016), and this is in agreement with the Haynes et al. (2018) distance of 16.7 ± 3.3 Mpc from the Masters (2005) flow model. NGC 3510 has clearly undergone an interaction that stretched its stellar arms and distorted its H I (Figure 11), and AGC 219369 is the nearest object to it (angular separation of $12\farcm2$, which corresponds to only 59 ± 12 kpc at a distance of 16.7 Mpc), so given the ambiguity on the distance it is reasonable to consider that AGC 219369 may have a distance of 16.7 Mpc as well.

The H I tail is significantly more substantial on the north side of NGC 3510, but tidal interactions usually produce two tidal tails which may or may not be similar sizes based on the parameters of the interaction (Duc & Bournaud 2008). We can consider whether the H I that formed the southern tail may have concentrated into a more massive object at its end and separated from it, producing AGC 219369, or whether AGC 219369 originally came from the larger tail and the southern tail was always short. In spite of the motion that the curvature of the H I tails suggests, NGC 3510 is very edge on, and Figure 12 confirms that the rotation axis is roughly perpendicular to the line of sight. This makes it particularly difficult to evaluate the state of the stellar disk, which otherwise may have provided clues about the interaction. Although they are not pictured in Figure 11, there are three other galaxies with similar heliocentric velocities nearby: UGC 6102 ($V_h = 697 \pm 35$ km s^{-1} from Haynes et al. 2018), UGCA 225 ($V_h = 647 \pm 22$ km s^{-1} from Haynes et al. 2018), and NGC 3486 ($V_h = 678 \pm 1$ km s^{-1} from Springob et al. 2005). UGC 6102 is a dwarf irregular galaxy with an angular separation of about $27'$ directly west from AGC 219369. UGCA 225 is a Blue Compact Dwarf located about $31'$ to the northeast of AGC 219369, and is actively forming stars (Cairós et al. 2001). NGC 3486 is a spiral galaxy located $49'$ to the northwest of AGC 219369, and is of comparable H I mass to NGC 3510 (Haynes et al. 2018).

In Figure 13, we can see that the H I distribution of AGC 219369 appears to be round, as is the optical component, which would suggest dynamical stability. The surface brightness profiles of AGC 219369are plotted in Figure 4, with scale bars for physical units corresponding to the reported ALFALFA distance of 9.2 Mpc (Haynes et al. 2018). The surface brightness profile in g follows an exponential law very closely, and results in a central surface brightness in g of 25.00 ± 0.03 mag arcsec^{-2}. The $(g - r)$ color of 0.08 ± 0.03 indicates it is quite blue. Due to the uncertainty in the distance to AGC 219369, properties that do not depend on distance are listed in Table 3, and properties that are distance-dependent have been calculated for both 9.2 Mpc and 16.7 Mpc (the distance of NGC 3510) and are listed in Table 4. While both sets of values are listed for completeness, AGC 219369 is assumed to be at the distance of NGC 3510 for the rest of this work. Under this assumption, the effective radius of AGC 219369, $17\farcs43 \pm 5\farcs36$, would correspond to 1.41 ± 0.52 kpc. AGC 219369 is the smallest AD-TDG candidate in this study, with an ALFALFA H I mass of only $(5.91 \pm 2.43) \times 10^7$ $M_\odot$ and an estimated stellar mass of $(4.76 \pm 0.44) \times 10^6$ $M_\odot$. This gives an H I-to-stellar mass ratio of 12.42 ± 5.28. A dynamical mass of $(4.72 \pm 1.81) \times 10^8$ $M_\odot$ leads to a dynamical-to-gas mass ratio of 9.00 ± 5.06.

4.3. AGC 229398

AGC 229398 is the farthest and most massive AD of the set, with a distance of 104.0 ± 2.3 Mpc and an H I mass of

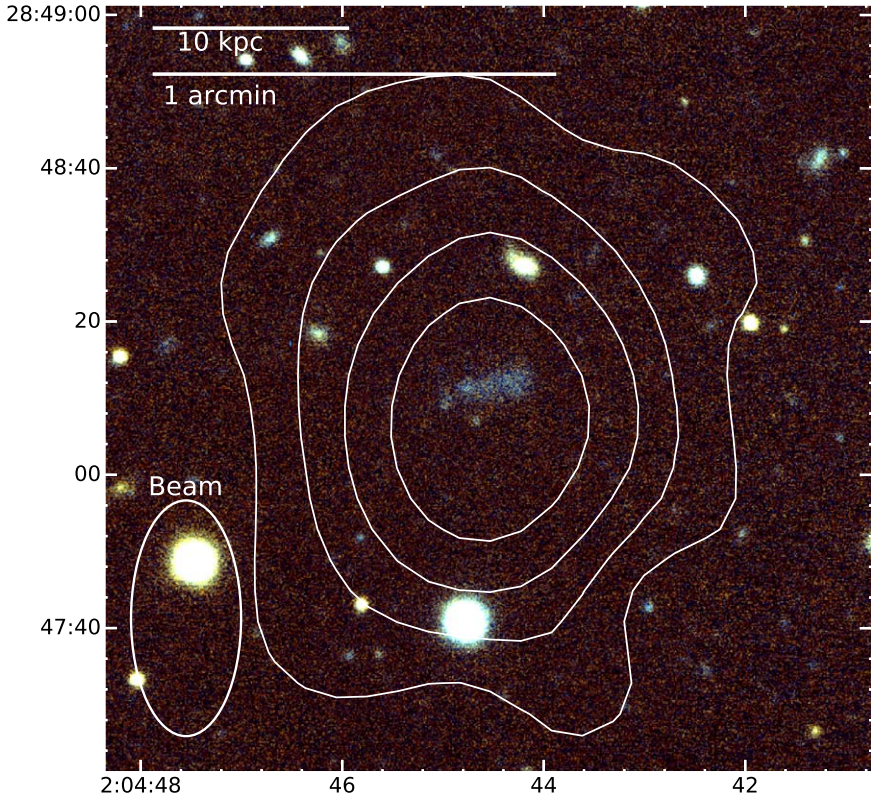

Figure 10. WIYN 3.5 m $g' + r'$-band composite image of AGC 123216, with WSRT H I column density contours at $N_{\rm H\,I} = (0.1, 0.5, 1.2, 2.4) \times 10^{20}$ cm^{-2}. The stellar component at the center is extremely blue and elongated in the east–west direction, while the H I distribution is rounder.

Table 2
Measured and Derived Properties of AGC 123216

Property (Units)	Value	Property (Units)	Value
R.A. [h m s, J2000]	02 04 44.6	Decl. [°′″, J2000]	+28 48 11.28
V_h'[km s^{-1}]	5111 ± 14	$N_{\rm H\,I,peak}$ [10^{20} cm^{-2}]	5.02
S_{21}' [Jy km s^{-1}]	0.38 ± 0.05	S_{21} [Jy km s^{-1}]	0.34 ± 0.03
$M_{\rm HI}'$ [10^8 $M_\odot$]	4.45 ± 0.79	$M_{\rm H\,I}$ [10^8 $M_\odot$]	3.98 ± 0.62
$M_{\rm gas}'$ [10^8 $M_\odot$]	5.91 ± 1.05	$M_{\rm gas}$ [10^8 $M_\odot$]	5.30 ± 0.83
$R_{\rm H\,I}$ [kpc]	7.69 ± 1.06	Inclination [°]	45 ± 5
R_e [kpc]	1.83 ± 0.04	R_d [kpc]	2.32 ± 0.05
$\mu_{g,0}$ [mag arcsec^{-2}]	24.86 ± 0.03	$\mu_{r,0}$ [mag arcsec^{-2}]	25.05 ± 0.08
m_g [mag]	20.80 ± 0.04	m_r [mag]	20.91 ± 0.11
M_g [mag]	−13.44 ± 0.08	M_r [mag]	−13.33 ± 0.13
(g–r) [mag]	−0.11 ± 0.12	M_* [10^6 $M_\odot$]	3.86 ± 1.24
$M_{\rm bary}'$ [10^8 $M_\odot$]	5.96 ± 1.05	$M_{\rm dyn}$ [10^9 $M_\odot$]	2.33 ± 0.82
$M_{\rm HI}'/L_g$	17.04 ± 3.39	$M_{\rm HI}'/L_r$	28.80 ± 6.32
$M_{\rm HI}'/M_*$	115.28 ± 42.20	$M_{\rm dyn}/M_{\rm gas}$	4.40 ± 1.70

Note. R.A.and decl. are listed for the optical component of AGC 123216. Properties marked with a $'$ are derived from ALFALFA measurements. Inclination is measured from the H I gas distribution, not the optical component. $M_{\rm dyn}$ is calculated using W_{20}' and D' from ALFALFA data and $R_{\rm H\,I}$ and inclination from WSRT data, as described in Sections 3.2 and 3.3.

$(1.91 \pm 0.22) \times 10^9$ $M_\odot$ (Haynes et al. 2018). It has two potential parent galaxies, of which UGC 6989 is the most distant potential parent in the sample (Figure 14). While the H I distribution is round, the optical component of AGC 229398

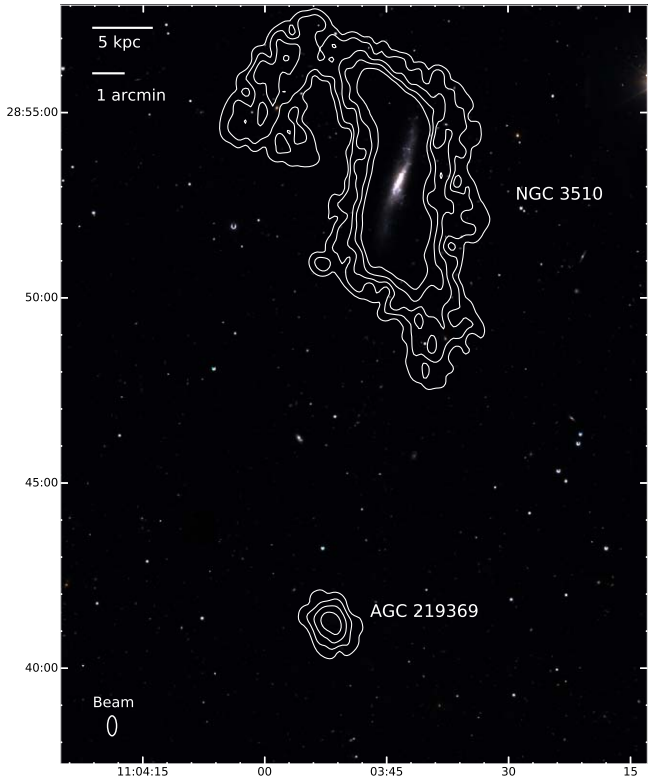

Figure 11. WIYN 3.5 m $g' + r'$-band composite image showing the full-field view of AGC 219369 (bottom), including potential parent NGC 3510 (top). There are WSRT H I column density contours at $N_{\rm H\,I} = (0.1, 0.5, 1.2, 2.4, 4.5) \times 10^{20}$ cm^{-2} superimposed in white. The physical scale bar is calculated for a distance of 9.2 Mpc.

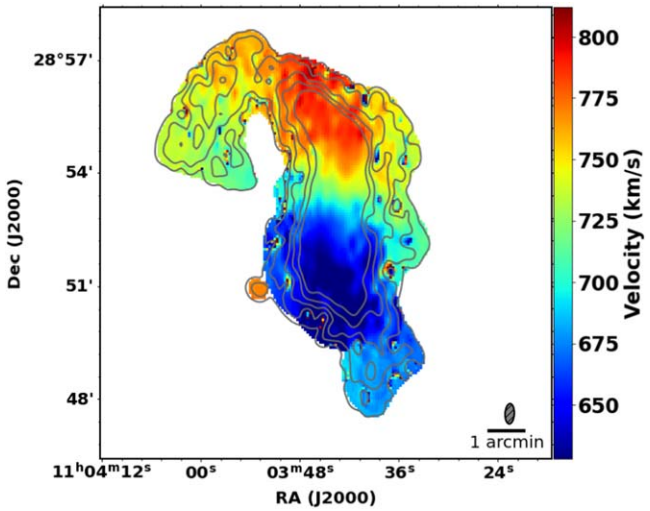

Figure 12. NGC 3510 moment one map from WSRT imaging, with WSRT H I column density contours superimposed in dark gray. Contour levels are the same as in Figure 11.

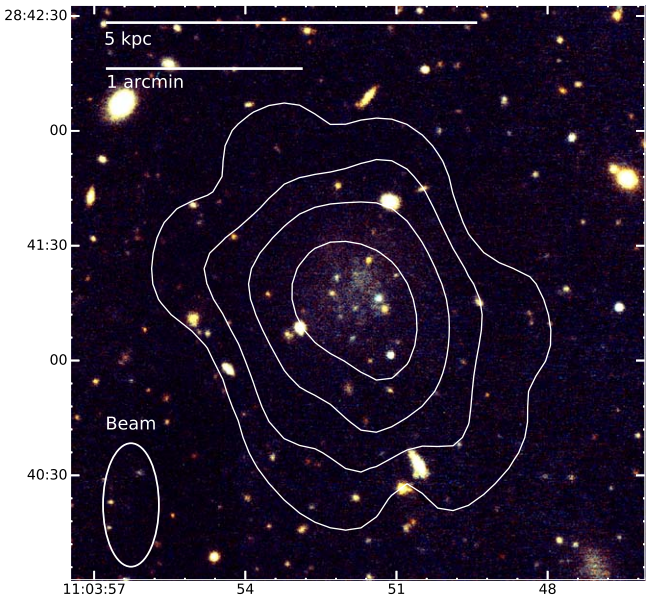

Figure 13. WIYN 3.5 m $g' + r'$-band composite image of AGC 219369, with WSRT H I column density contours at $N_{\rm H\,I} = (0.1, 0.5, 1.2, 2.4) \times 10^{20}$ cm^{-2} superimposed in white. The physical scale bar is calculated for a distance of 9.2 Mpc.

itself is elongated in the east–west direction (Figure 15). There also appears to be a small knot of stellar emission to the northeast.

The spiral galaxy KUG 1158+216, which is located to the south of AGC 229398, is the closest potential parent galaxy in distance, heliocentric velocity, and angular separation. The distance given by the ALFALFA survey is 110.1 ± 2.3 Mpc, the heliocentric velocity difference is 423 ± 126 km s^{-1}, and the projected separation on the sky is 102 ± 2 kpc (Haynes et al. 2018). There is a faint stellar tail extending from the eastern side that may be the remains of a tidal interaction (left panel of Figure 16). We do not have maps of the H I emission for KUG 1158+216, so we are unable to examine the neutral gas distribution for signs of tidal distortion in the direction of AGC 229398.

Table 3
Distance-independent Measured Properties of AGC 219369

Property (Units)	Value	Property (Units)	Value
R.A. [h m s, J2000]	11 03 51.8	Decl. [° ′ ″, J2000]	+28 41 17.8
V'_h [km s^{-1}]	667 ± 4	$N_{\rm H\,I,peak}$ [10^{20} cm^{-2}]	4.40
S'_{21} [Jy km s^{-1}]	0.90 ± 0.04	S_{21} [Jy km s^{-1}]	0.60 ± 0.03
$R_{\rm H\,I}$ [arcsec]	32 ± 3	Inclination [°]	53 ± 2
R_e [arcsec]	17.43 ± 5.36	R_d [arcsec]	10.35 ± 3.18
$\mu_{g,0}$ [mag arcsec^{-2}]	25.00 ± 0.03	$\mu_{r,0}$ [mag arcsec^{-2}]	25.16 ± 0.02
m_g [mag]	18.12 ± 0.02	m_r [mag]	18.04 ± 0.02
$(g–r)$ [mag]	0.08 ± 0.03	$M'_{\rm HI}/M_*$	12.42 ± 5.23
$M'_{\rm HI}/L_g$	3.38 ± 1.93	$M'_{\rm HI}/L_r$	4.78 ± 2.73

Note. R.A. and decl. are listed for the optical component of AGC 219369. Properties marked with a ′ are derived from ALFALFA measurements. Inclination is measured from the H I gas distribution, not the optical component.

Table 4
Distance-dependent Measured Properties of AGC 219369

Distance (Mpc)	9.2 ± 2.2	16.7 ± 3.3
$M'_{\rm HI}$ [10^7 $M_\odot$]	1.79 ± 0.88	5.91 ± 2.43
$M'_{\rm gas}$ [10^7 $M_\odot$]	2.39 ± 1.17	7.87 ± 3.23
$M_{\rm H\,I}$ [10^7 $M_\odot$]	1.20 ± 0.59	3.94 ± 1.62
$M_{\rm gas}$ [10^7 $M_\odot$]	1.59 ± 0.78	5.24 ± 2.15
$R_{\rm H\,I}$ [kpc]	1.40 ± 0.36	2.55 ± 0.56
R_e [kpc]	0.78 ± 0.24	1.41 ± 0.52
R_d [kpc]	0.46 ± 0.14	0.84 ± 0.31
M_g [mag]	-11.70 ± 0.52	-12.99 ± 0.43
M_r [mag]	-11.78 ± 0.52	-13.08 ± 0.43
M_* [10^6 $M_\odot$]	1.44 ± 0.14	4.76 ± 0.44
$M'_{\rm bary}$ [10^7 $M_\odot$]	2.53 ± 1.17	8.34 ± 3.23
$M_{\rm dyn}$ [10^8 $M_\odot$]	2.60 ± 1.06	4.72 ± 1.81
$M_{\rm dyn}/M_{\rm gas}$	16.34 ± 10.42	9.00 ± 5.06

Note. Properties marked with a ′ are derived from ALFALFA measurements. $M_{\rm dyn}$ is calculated using W'_{20} ALFALFA data and $R_{\rm H\,I}$ and inclination from WSRT data, as described in Sections 3.2 and 3.3.

UGC 6989 is a spiral galaxy some distance away from AGC 229398, with a projected separation of 482 ± 11 kpc. The ALFALFA survey lists the distance of UGC 6989 as 96.0 ± 2.4 Mpc, but there are some discrepancies between other measurement methods. The redshift-independent Tully–Fisher measurement from the Cosmicflows-4 survey, which uses the relationship between H I line widths (i.e., rotation rates) and galaxy luminosities to measure the distances to almost 10,000 spiral galaxies, is 79.8 ± 8.9 Mpc (Kourkchi et al. 2020), which would remove it from consideration as a possible parent. The H I distribution and spiral disk of UGC 6989 do not show much sign of disturbance (right panel of Figure 16), though AGC 229398 is far enough that if it had come from UGC 6989, enough time may have passed for it to restabilize.

The measured properties of AGC 229398 can be found in Table 5, and Figure 5 shows the surface brightness profiles. It has the largest effective radius, with $r_e = 9.05 \pm 1.10$ kpc, and a central surface brightness in g of 23.84 ± 0.13 mag arcsec^{-2}. The $(g - r)$ color of 0.35 ± 0.15 mag is the reddest of the AD-TDG candidates. The H I mass measured by WSRT is significantly smaller than the one measured by ALFALFA,

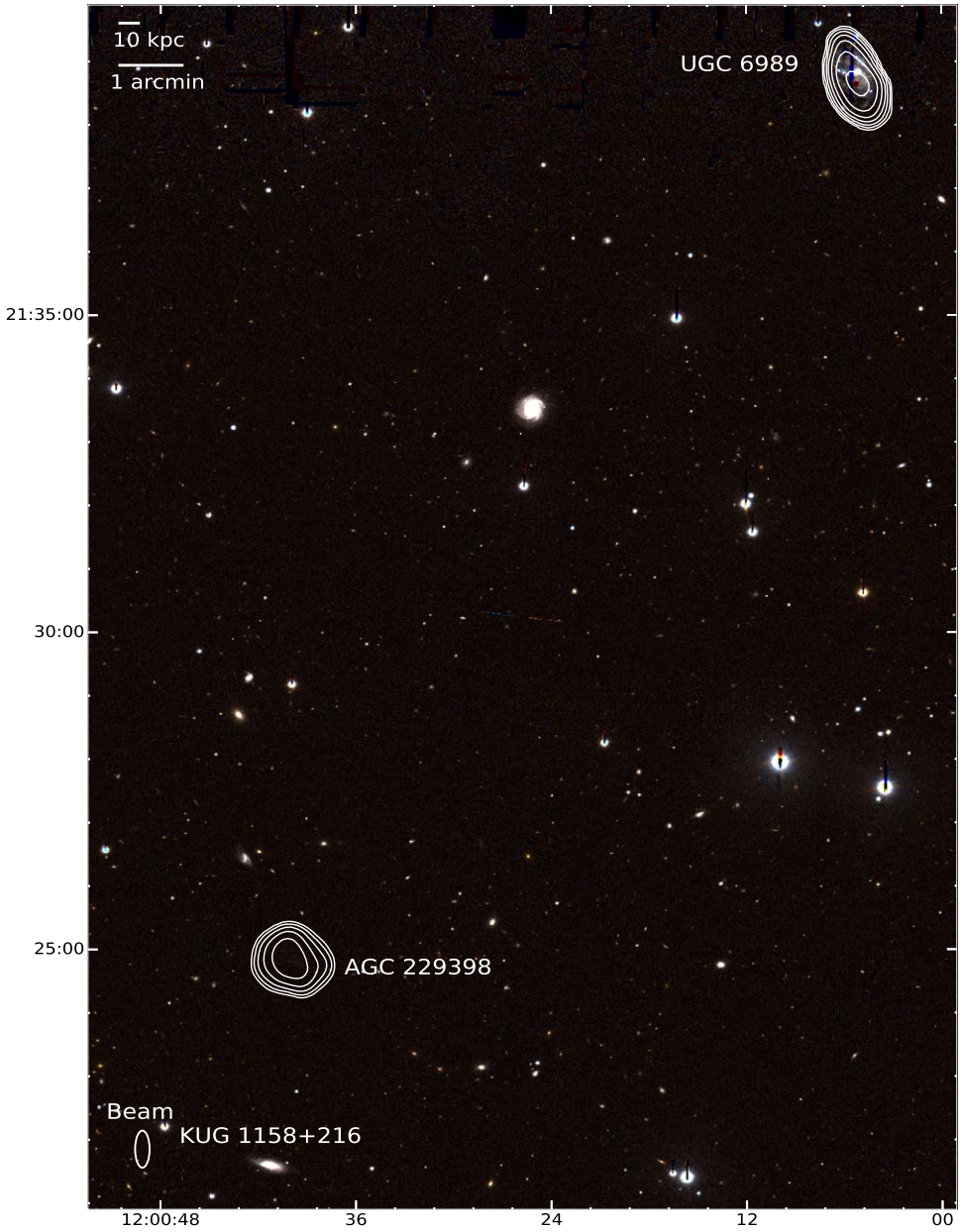

Figure 14. WIYN 3.5 m $g' + r'$-band composite image showing the full-field view of AGC 229398 (lower left) with potential parents UGC 6989 (upper right) and KUG 1158+216 (below label). There are WSRT H I column density contours at $N_{\rm H\,I} = (0.1, 0.2, 0.4, 0.8, 1.6, 3.2, 6.4) \times 10^{20}$ cm^{-2} superimposed in white. Note that the prominent spiral galaxy near the center of the image is CGCG 127-132, which has a heliocentric velocity of 14,457 $\pm$ 4 km s^{-1} and is not associated with the objects of interest in this paper (Albareti et al. 2017).

which suggests that ALFALFA may be detecting diffuse gas that is distributed over a larger area. AGC 229398 also has the second highest stellar mass of $(9.78 \pm 4.82) \times 10^7\ M_\odot$, though this is still small compared to the gas content, giving a fairly high H I-to-stellar mass ratio of 19.54 ± 9.92. The estimated dynamical mass is $(1.64 \pm 0.39) \times 10^9\ M_\odot$, and it has a low dynamical-to-gas mass ratio of 1.52 ± 0.41.

4.4. AGC 333576

AGC 333576 has one obvious potential parent galaxy, NGC 7775. NGC 7775 is a spiral galaxy with chaotic stellar arms and a bright area in the lower right corner of the galaxy, which may be a massive star formation region (Figure 17). NGC 7775's H I distribution reveals a clear distortion in the direction of AGC 333576 (Figure 17), and the optical image shows a tidal tail extending from the north side and curving toward AGC 333576 (Figure 18, left). According to the H I heliocentric velocities from Haynes et al. (2018), both objects are 93.9 ± 4.3 Mpc away, and this is in agreement with other redshift-independent measurements for NGC 7775 (96.50 ± 19 Mpc from Theureau et al. 2007). The optical component of AGC 333576 is relatively rounded, though there appear to be two distinct branches on the left side and there are clear knots of brighter stars (right panel of Figure 18). The surrounding H I is slightly elongated along the northwest/southeast axis. In the course of investigating this system, we have also found the elliptical galaxy to the upper left of AGC 333576, WISEA J235250.49+284555.2. Not much is known about this galaxy, and it should be noted that this galaxy has been mistakenly cross-identified with AGC 333576 in the

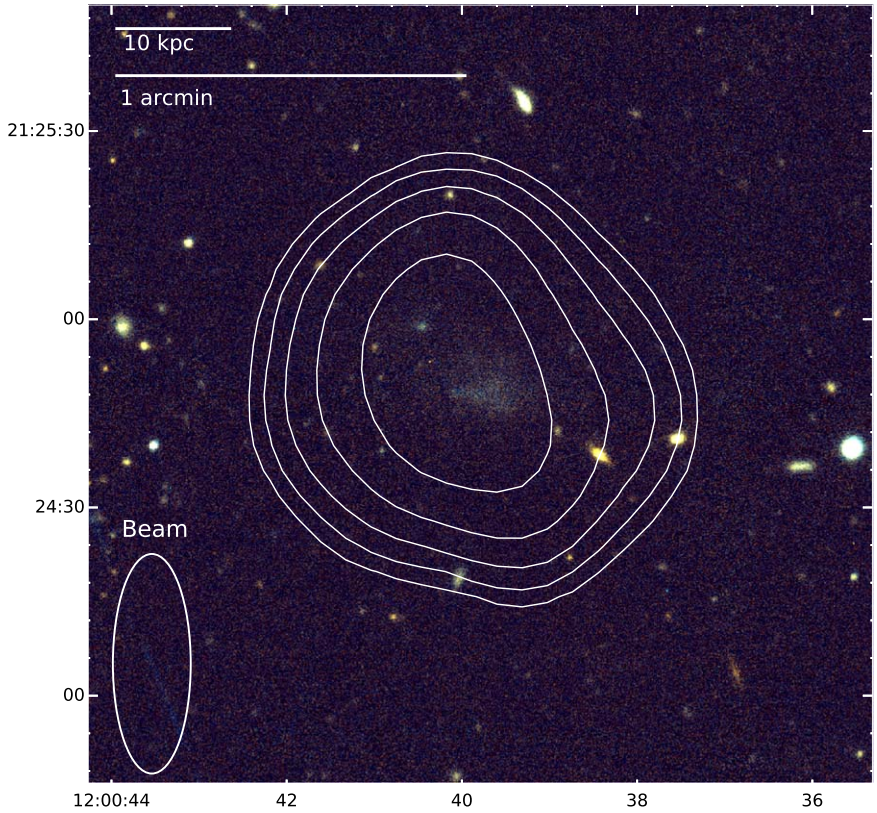

Figure 15. WIYN 3.5 m $g' + r'$-band composite image of AGC 229398, with WSRT H I column density contours at $N_{\rm H\,I} = (0.1, 0.2, 0.4, 0.8, 1.6) \times 10^{20}$ cm^{-2} in white.

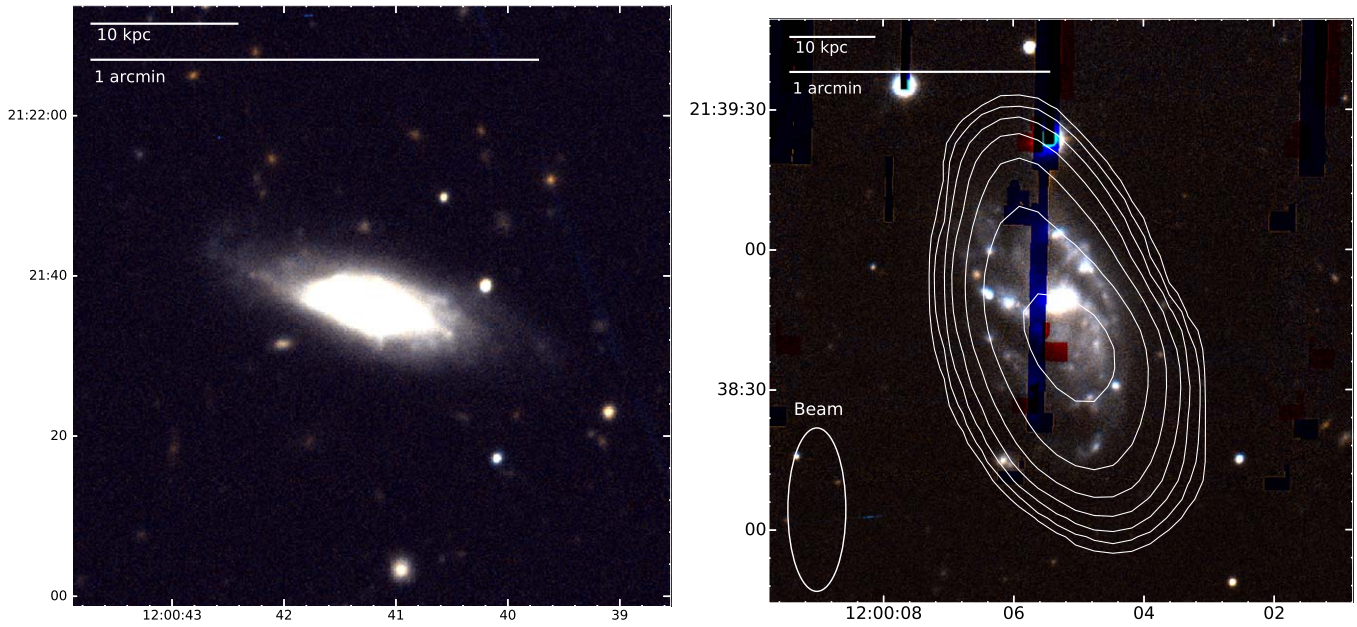

Figure 16. WIYN 3.5 m $g' + r'$-band composite imaging for the potential parents of AGC 229398. Left: KUG 1158+216, scaled to show the faint extension of stellar emission on the left. Right: UGC 6989, with WSRT H I column density contours at $N_{\rm H\,I} = (0.1, 0.2, 0.4, 0.8, 1.6, 3.2, 6.4) \times 10^{20}$ cm^{-2} in white. Due to the large angular separation from AGC 229398 and the smaller field of view of pODI, UGC 6989 was located at the edge of the CCD, which resulted in several detector artifacts in the image.

NASA/IPAC Extragalactic Database, so some of the information listed there is actually data associated with the AD. It has a measured heliocentric velocity of 7157 ± 24 km s^{-1} (Huchra et al. 2012), which places it at a similar distance to the other two galaxies in this system, and it is $105'' \pm 0.''125$ away from AGC 333576 on the sky, or roughly 48 ± 2 kpc. Because WISEA J235250.49+284555.2 is an elliptical, it likely did not have enough H I gas to be included in the ALFALFA catalog and thus be identified as a potential parent galaxy; however, it may still be involved in the interactions of this system.

The measured properties of AGC 333576 are listed in Table 6, and Figure 6 displays the surface brightness profiles. It has a central surface brightness in g of 24.57 ± 0.02 mag arcsec^{-2}, an effective radius of 4.40 ± 0.05 kpc, and a

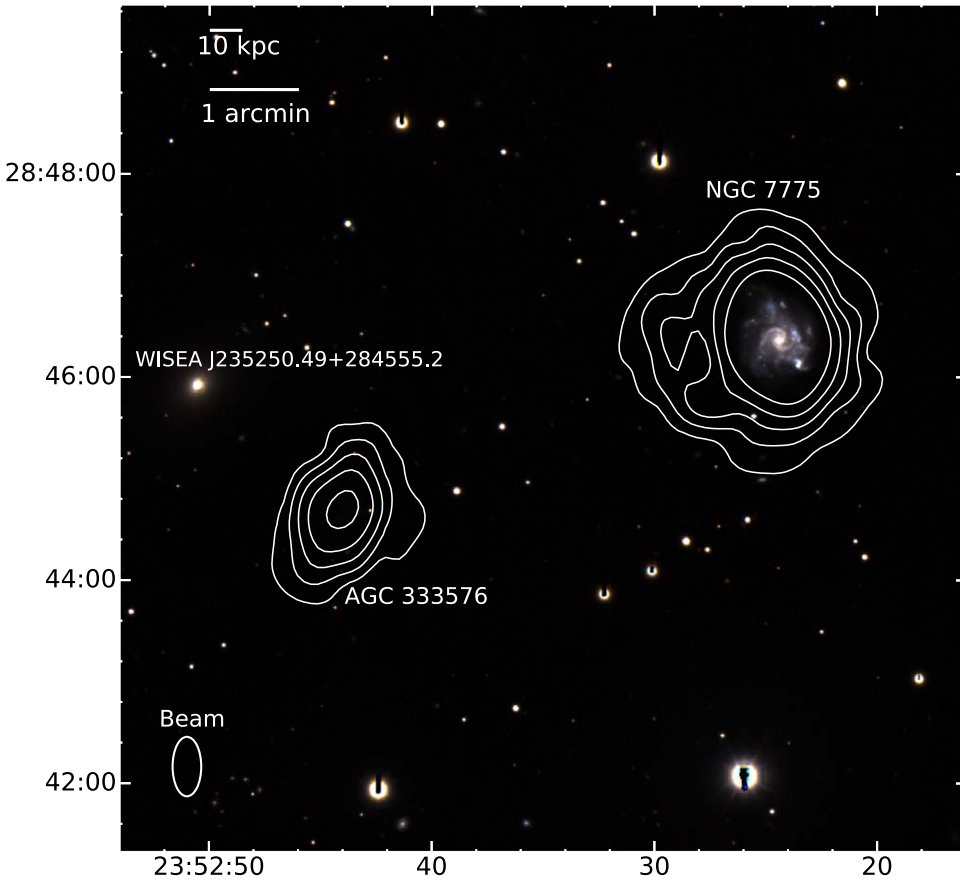

Figure 17. WIYN 3.5 m $g' + r'$-band composite image showing the full-field view of AGC 333576 and potential parent NGC 7775. There are WSRT H I column density contours at $N_{\rm H\,I} = (0.1, 0.5, 1.2, 2.4, 4.5) \times 10^{20}$ cm^{-2} superimposed in white. The nearby elliptical galaxy WISEA J235250.49+284555.2 is also labeled.

$g - r$ color of 0.21 ± 0.03 mag. AGC 333576 is estimated as having a stellar mass of $(1.64 \pm 0.12) \times 10^8\ M_\odot$, the largest in the set, which gives it a H I-to-stellar mass ratio of 7.60 ± 1.28. The dynamical mass of $(1.90 \pm 0.37) \times 10^9\ M_\odot$ gives a very low dynamical-to-gas mass ratio of 1.07 ± 0.27.

5. Discussion

5.1. Basic TDG Properties

Kaviraj et al. (2012) report several general characteristics of TDGs based on their statistical study of candidate TDGs. This study selects objects that appear in SDSS images of galaxy mergers and have been identified as separate photometric objects by the SDSS processing software and have a tidal stellar tail that connects the object to the parent. These criteria mean that younger objects are favored. Some of these objects likely will not become independent self-gravitating objects, so they are only TDG candidates. It is important to consider which characteristics may change as a TDG ages. The clearest example of this is that Kaviraj et al. (2012) report that 95% of TDG candidates were located within a projected distance of ~20 kpc from their progenitors. It is likely that they have simply not had enough time to move much farther, as tidal tails are only present for a few hundred million years after the first pericentric encounter of the interacting galaxies (Bournaud & Duc 2006).

TDGs tend to be bluer than their parents (with a median offset of 0.3 mag) due to the star formation triggered by the turbulence of the tidal interaction (Kaviraj et al. 2012). It may be the case that as TDGs age, this color differential becomes less pronounced, though they may also remain quite blue. All of the ADs in this sample are markedly blue, and bluer than their potential parents, which may indicate that the stellar populations present were recently formed. However, low-surface-brightness galaxies as a population tend to be blue for reasons independent of hosting a primarily young stellar population (McGaugh 1992; de Blok et al. 1995).

The systems in the Kaviraj et al. (2012) sample primarily involve galaxies that are clearly in the process of interacting—there are at least two galaxies fairly close to each other on the sky, showing some sort of stellar distortion (see merger classification details in Darg et al. 2010). Bournaud & Duc (2006) conducted a set of numerical simulations of galaxy interactions with a variety of interaction parameters, in order to examine the merger scenarios in which TDGs are most likely to form and to survive long-term (which they defined as >1 Gyr). Based on the Bournaud & Duc (2006) simulations, the interactions most likely to produce long-lived TDGs are those between spiral galaxies with prograde orbits, where the mass of the companion galaxy is large enough to drive matter out of the main progenitor galaxy (at least one-fourth the mass of the progenitor), but not so massive that the material falls back onto the companion (less than 8 times more massive than the progenitor). In cases where a clearly merging system is present, we might be able to use these expected properties to evaluate whether an interaction is likely to have produced a long-lived TDG. However, most of the proposed parents in this study

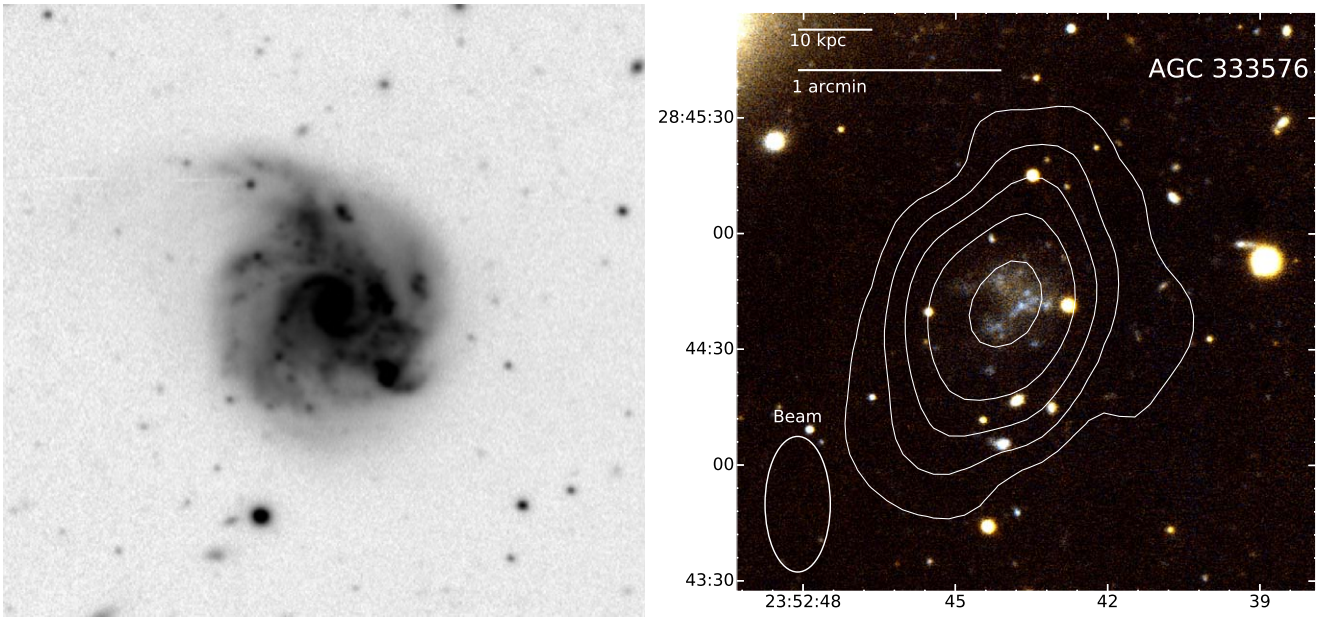

Figure 18. Left: WIYN 3.5 m composite $g' + r'$-band summed image of NGC 7775 in grayscale, inverted to highlight the tidal tail at the top. Right: WIYN 3.5 m $g' + r'$-band composite image of AGC 333576, with same H I column density contours as Figure 17 in white.

Table 5
Measured and Derived Properties of AGC 229398

Property (Units)	Value	Property (Units)	Value
R.A. [h m s, J2000]	12 00 39.8	Decl. [° ′ ″, J2000]	+21 24 47.6
v_h' [km s^{-1}]	6965 ± 14	$N_{\rm H\,I,peak}$ [10^{20} cm^{-2}]	3.95
S_{21}' [Jy km s^{-1}]	0.75 ± 0.04	S_{21} [Jy km s^{-1}]	0.32 ± 0.03
$M_{\rm HI}'$ [10^9 $M_\odot$]	1.91 ± 0.23	$M_{\rm H\,I}$ [10^8 $M_\odot$]	8.15 ± 1.11
$M_{\rm gas}'$ [10^9 $M_\odot$]	2.54 ± 0.31	$M_{\rm gas}$ [10^9 $M_\odot$]	1.09 ± 0.15
$R_{\rm H\,I}$ [kpc]	9.83 ± 1.53	Inclination [°]	66 ± 8
R_e [kpc]	9.05 ± 1.10	R_d [kpc]	0.95 ± 0.12
$\mu_{g,0}$ [mag arcsec^{-2}]	23.84 ± 0.13	$\mu_{r,0}$ [mag arcsec^{-2}]	24.48 ± 0.10
m_g [mag]	19.74 ± 0.11	m_r [mag]	19.39 ± 0.10
M_g [mag]	−15.35 ± 0.12	M_r [mag]	−15.69 ± 0.11
(g–r) [mag]	0.35 ± 0.15	M_* [10^7 $M_\odot$]	9.78 ± 4.82
$M_{\rm bary}'$ [10^9 $M_\odot$]	2.64 ± 0.31	$M_{\rm dyn}$ [10^9 $M_\odot$]	1.64 ± 0.39
$M_{\rm HI}'/L_g$	12.51 ± 1.99	$M_{\rm HI}'/L_r$	13.88 ± 2.10
$M_{\rm HI}'/M_*$	19.54 ± 9.92	$M_{\rm dyn}/M_{\rm gas}$	1.52 ± 0.41

Note. R.A. and decl. are listed for the optical component of AGC 229398. Properties marked with a ′ are derived from ALFALFA measurements. Inclination is measured from the H I gas distribution, not the optical component. $M_{\rm dyn}$ is calculated using W_{20}' and D' from ALFALFA data and $R_{\rm H\,I}$ and inclination from WSRT data, as described in Sections 3.2 and 3.3.

Table 6
Measured and Derived Properties of AGC 333576

Property (Units)	Value	Property (Units)	Value
R.A.[h m s, J2000]	23 52 43.6	Decl.[° ′ ″, J2000]	+28 44 42.5
V_h' [km s^{-1}]	7031 ± 13	$N_{\rm H\,I,peak}$ [10^{20} cm^{-2}]	5.89
S_{21}' [Jy km s^{-1}]	0.60 ± 0.04	S_{21} [Jy km s^{-1}]	0.64 ± 0.05
$M_{\rm HI}'$ [10^9 $M_\odot$]	1.25 ± 0.19	$M_{\rm H\,I}$ [10^9 $M_\odot$]	1.33 ± 0.21
$M_{\rm gas}'$ [10^9 $M_\odot$]	1.66 ± 0.25	$M_{\rm gas}$ [10^9 $M_\odot$]	1.77 ± 0.28
$R_{\rm H\,I}$ [kpc]	16.73 ± 1.57	Inclination [°]	57 ± 2
R_e [kpc]	4.40 ± 0.05	R_d [kpc]	3.94 ± 0.04
$\mu_{g,0}$ [mag arcsec^{-2}]	24.57 ± 0.02	$\mu_{r,0}$ [mag arcsec^{-2}]	24.45 ± 0.02
m_g [mag]	18.48 ± 0.02	m_r [mag]	18.27 ± 0.02
M_g [mag]	−16.38 ± 0.10	M_r [mag]	−16.60 ± 0.10
(g–r) [mag]	0.21 ± 0.03	M_* [10^8 $M_\odot$]	1.64 ± 0.12
$M_{\rm bary}'$ [10^9 $M_\odot$]	1.82 ± 0.25	$M_{\rm dyn}$ [10^9 $M_\odot$]	1.90 ± 0.37
$M_{\rm HI}'/L_g$	3.18 ± 0.59	$M_{\rm HI}'/L_r$	4.00 ± 0.75
$M_{\rm HI}'/M_*$	7.60 ± 1.28	$M_{\rm dyn}/M_{\rm gas}$	1.07 ± 0.27

Note. R.A. and decl. are listed for the optical component of AGC 333576. Properties marked with a ′ are derived from ALFALFA measurements. Inclination is measured from the H I gas distribution, not the optical component. $M_{\rm dyn}$ is calculated using W_{20}' and D' from ALFALFA data and $R_{\rm H\,I}$ and inclination from WSRT data, as described in Sections 3.2 and 3.3.

appear to be single galaxies, well separated from the other potential parents and with generally undisturbed stellar distributions. In some cases the interactions could have progressed enough that the parent systems have merged completely; learning about the interaction would then require further analysis of stellar populations, star formation histories, and gas dynamics.

Simulations indicate that the masses of TDGs are usually a few percent of the baryonic mass of their parents, and rarely exceed 10% of that mass (Bournaud & Duc 2006). We can estimate the baryonic mass of the parent galaxies as follows: $M_{\rm atomic}$ is estimated to account for the presence of helium and other elements, so $M_{\rm atomic}' = 1.33 \times M_{\rm HI}'$, where $M_{\rm HI}'$ is from the ALFALFA survey (Haynes et al. 2018) as calculated by Equation (1). The stellar masses were estimated by Durbala et al. (2020). They calculated stellar masses using CMLRs between photometry and mass for SDSS optical photometry and infrared photometry from the reprocessed Wide-field Infrared Survey Explorer (WISE; Wright 2010) catalog known as unWISE (Lang 2014), and checked the agreement with stellar masses

derived from spectral energy distribution fitting in the Galaxy Evolution Explorer (GALEX)-SDSS-WISE Legacy Catalog 2 (GSWLC-2; Salim et al. 2016, 2018). We used their estimates from the Taylor relationship, noting that they are generally more conservative than those from other calibrations, which means that the mass ratios calculated are on the higher end. As most of the potential parent galaxies are spiral galaxies, molecular gas mass must be taken into account when estimating the baryonic mass. Young & Scoville (1991) report median H_2-to-H I mass ratios for different types of spiral galaxies, which we used to estimate $M'_{\rm molecular}$ for each potential parent based on the type listed on NED (NASA/IPAC Extragalactic Database (NED) 2019). For galaxies that did not have a specific type listed, a mass ratio of one was used. Young & Scoville (1991) note that early-type galaxies have higher H_2-to-HI mass ratios than late-types, so we used a ratio of 2.5 for NGC 807. Then, $M'_{\rm bary} = M'_{\rm atomic} + M_* + M'_{\rm molecular}$. This calculation was not done for MRK 365, as we do not have mass estimates for it. Most of the AD-TDG candidates do not exceed 5% of the baryonic mass of any individual potential parent. However, AGC 229398 has high mass ratios with respect to its potential parents (15.3% with UGC 6989 and 23.9% with KUG 1158+216), which seems to make it less likely that either galaxy is the parent; such an enormous removal of mass would cause major disruption to the parent, but these spirals appear to be relatively intact.

5.2. Context of Other TDGs

The sample of candidate TDGs to compare these candidates to is small, and the sample of confidently identified TDGs that have completely separated from their parent systems is even smaller. We have selected a comparison sample of likely TDGs identified in other studies that have similar measurements to those we have conducted for the AD-TDG candidates. These are AGC 749170, AGC 208457, NGC 5557-E1, NGC 5557-E2, NGC 5291N, NGC 5291S, NGC 5291SW, NGC 7252E, NGC 7252NW, VCC 2062, and HCG 16-LSB1.

1. In Lee-Waddell et al. (2012, 2014, 2016), two ADs have been identified as TDGs, and so are included in the discussion of AD-TDGs as a group. The analyses in those papers were carried out with measurements from the Giant Metrewave Radio Telescope (GMRT), which has a higher spatial resolution than the Arecibo telescope. A higher-resolution beam does a better job of mapping the fine gas structure, but does not capture the more diffuse surrounding gas. Lee-Waddell et al. (2012) note that the GMRT maps capture less than 40% of the flux density of the ALFALFA measurements and therefore the ALFALFA gas mass. In the interest of comparing these sources to the work done here, we use the ALFALFA survey data from Haynes et al. (2018) when discussing the total gas mass content of the galaxy and the GMRT values reported by Lee-Waddell et al. (Lee-Waddell et al. (2012, 2014, 2016)) for the dynamical-to-gas mass ratio. The estimates reported for these objects do not include an asymmetric drift correction.
   (a) AGC 749170 has an extremely high gas-mass-to-light ratio (>1000; Lee-Waddell et al. 2014). Lee-Waddell et al. 2014 used stellar population models to estimate its age at 6.3–12 Myr, which is very young for a galaxy's global population and suggests that there are very few preexisting stars in AGC 749170. This stellar population age estimate depends on an estimated $g - i$ range due to a nondetection in the i band. Additionally, in order to reach its present separation of at least 90 kpc (from the angular distance projection on the sky, though the true distance is likely greater) in only 12 Myr, AGC 749170 would need to travel at a speed of at least 7300 km s^{-1}, which would be unreasonably fast. The lack of a gaseous tail stretching from AGC 749170 also seems to imply an older age, because forming such a large mass of H I would require a significant tail which would take at least a few hundred million years to fade below the detection limits. On the other hand, the tail may be present but very diffuse, and therefore not captured in the higher-resolution GMRT images.
   (b) AGC 208457 appears to have the last remnants of an H I tail connecting it to its potential parent, the spiral galaxy NGC 3169, based on H I maps from Lee-Waddell et al. (2012). This, in combination with the elongation of the H I in AGC 208457, suggests that the TDG may not have reached full dynamical equilibrium yet, so the estimated dynamical mass (and thus the dark matter content) may not be accurate. AGC 208457 has an estimated age range of 6–2600 Myr, based on the age of the stellar component using a Chabrier initial mass function (Lee-Waddell et al. 2016). Follow-up spectroscopy of AGC 208457 confirmed that it has the enriched metallicity indicative of a tidal origin (Lee-Waddell et al. 2018).
2. Duc et al. (2014) identified two objects likely to be TDGs around the elliptical galaxy NGC 5557: NGC 5557-E1 and NGC 5557-E2. Using spectrophotometric methods, they analyzed NGC 5557-E1 and came to the conclusion that its near-solar oxygen abundance was typical of galaxies 10 times more massive, and therefore the material was preenriched. Deep optical imaging from MegaCam on the Canada–France–Hawaii Telescope (CFHT) revealed that NGC 5557-E1 was located in a large and diffuse stellar stream. They considered that NGC 5557-E1 could be the remnant of a preexisting satellite galaxy that had been tidally disturbed, but the remains of such an interaction would be redder, and the surrounding tidal tails would likely have an "S shape" (Duc et al. 2014). The blue color of NGC 5557-E1 and the straightness of the tail precluded this as a likely origin scenario, and so Duc et al. (2014) concluded that it was a TDG formed during a tidal interaction. NGC 5557-E2 is located farther along this tail and likely originated in the same interaction. They estimated the age of these objects to be between 2 and 4 Gyr, which would make them much older than any TDGs previously identified. Both "older" TDGs have larger effective radii than other dwarf galaxies of comparable stellar mass, in accordance with other, younger TDGs that have been identified by their tidal tails (Duc et al. 2014). Duc et al. (2014) suggested that the larger radii may be used as an additional tool to aid in distinguishing TDGs from dwarf satellite galaxies without spectroscopy.
3. Lelli et al. (2015) performed new observations and analysis for a sample of six previously identified candidate TDGs: NGC 5291N, NGC 5291S, NGC 5291SW, NGC 7252E, NGC 7252NW, and

VCC 2062. They also cited additional photometric properties of the latter three compiled in Duc et al. (2014). Lelli et al. (2015) found that NGC 7252E and NGC 7252NW are comprised of preenriched material and lack a significant dark matter mass, and are therefore genuine TDGs, and reference similar results for the three objects around NGC 5291 (Bournaud et al. 2007) and for VCC 2062 (Duc et al. 2007).

4. HCG 16-LSB1 is located at the end of an H I tail extending out of the galaxy HCG 16 c, which is part of the complex galaxy interactions occurring in HCG 16. Román et al. (2021) concluded that HCG 16-LSB1 has a high metallicity that is compatible with it being a newly formed TDG. They estimated a dynamical mass range of $(1.2–4.1) \times 10^9\ M_\odot$, with the further caveat that HCG 16-LSB1 may be too young to be gravitationally bound (Román et al. 2021). Even the low end of this range would indicate a higher than expected amount of dark matter for a TDG, yet the object has clearly formed from enriched material at the end of a tidal tail. The mass and location of HCG 16-LSB1 at the end of a tidal tail make it very likely to have longevity based on the results of the simulations of Bournaud & Duc (2006), so it seems feasible that it will become gravitationally independent as a proper TDG in the future.

5.3. Dark Matter Content

The ratio of the dynamical (total) mass to the gas mass provides a measure of the dark matter content in a galaxy. To calculate the numerator in this ratio, we use the dynamical mass described in Section 3.3, which is calculated with Equation (3) and uses the ALFALFA velocity width and distance (W'_{20} and D' and the inclination and radius ($R_{\rm H\,I}$) derived from the WSRT data. Because the spatial values used to calculate dynamical mass (inclination and radius) are derived from spatial measurements from the WSRT data, we use the WSRT gas mass as the denominator in the dynamical-to-gas mass ratio. For our ADs, the stellar contribution to the mass is minimal, so we consider only the gas mass for the current discussion. TDGs are primarily composed of gas from the disk material of their progenitors, and so should contain very little dark matter and therefore are expected to have $M_{\rm dyn}/M_{\rm gas}$ near 1. Figure 19 shows the dynamical-to-gas mass ratios of the four candidate AD-TDGs in this sample in comparison to the values for the TDGs in Román et al. (2021), Lelli et al. (2015), and Lee-Waddell et al. (2016). To provide a comparison sample of non-TDG dwarf galaxies we have also plotted values for the dwarf irregular galaxies in the Local Group compiled by McConnachie (2012).

AGC 229398 and AGC 333576 have ratios that clearly place them in the regime of previously identified TDGs in the lower right corner of the plot, while AGC 219369 appears to be dark matter dominated (Figure 19). This suggests that AGC 219369 is unlikely to be a TDG. Instead, it may simply be a small dwarf galaxy that happens to be near a tidally disturbed spiral in the sky, or may have even interacted with it previously. AGC 123216's dynamical mass to gas mass ratio indicates a higher dark matter content than expected for an object of tidal origin, though it still has a lower amount of dark matter than most of the Local Group dwarf irregular galaxies. It is worth noting that while HCG 16-LSB1, which is a clearly tidal object, is located in the dark matter dominated portion of the plot, it is such a young object that it may not be dynamically stable yet. This means that the currently estimated dynamical mass may be larger than the actual total dynamical mass.

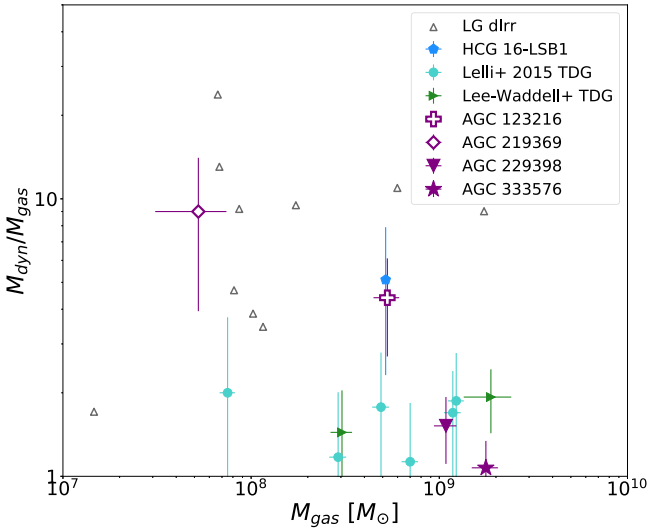

Figure 19. Comparison of dynamical-to-gas mass ratios for objects from this work (purple, various symbols) to the young TDG candidate HCG 16-LSB1 (Román et al. 2021; blue pentagon), AD-TDG candidates from Lee-Waddell et al. (2016; green right-pointing triangles), and TDG candidates from Lelli et al. (2015; turquoise circles). For the comparison of TDG properties to those of normal (non-TDG) dwarf galaxies, we have plotted a sample of Local Group dIrrs from McConnachie (2012; dark gray triangles). $M_{\rm gas}$ for the LG dIrrs is calculated using 1.33 × the H I mass reported in McConnachie (2012), and $M_{\rm dyn}$ uses the dynamical masses from the same paper supplemented by the total masses reported in Mateo (1998) when necessary. $M_{\rm gas}$ for the TDGs from Lelli et al. (2015) is the sum of $M_{\rm atomic}$ and $M_{\rm molecular}$ reported in that work. All objects that have been identified as TDGs have filled symbols, and those that are not TDGs have unfilled symbols.

5.4. Stellar Content

The four AD-TDG candidates studied in this work were selected from the larger ALFALFA AD sample in part because of their large H I-to-optical-light ratios. As previously mentioned, it is likely that ADs may not efficiently convert neutral H I to cold molecular gas (Wang et al. 2020), impacting their star formation rate. According to simulations, the critical column density threshold of H I for star formation is thought to range from $(3–10) \times 10^{20}$ cm^{-2} (Schaye 2004), depending on the local conditions. The critical surface density corresponds to a critical minimum pressure to trigger a transition to a cold phase, where the temperature of the gas drops and the H_2 formation rate increases in order to maintain the pressure, thereby increasing the fraction of molecular gas (Schaye 2004). The phase transition also causes gravitational instability in the gas cloud, which results in fragmentation and, eventually, star formation (Schaye 2004). If there is not a high enough column density (and therefore pressure) of neutral gas to cause the phase transition and increase the molecular gas fraction, the gas cloud does not become unstable and collapse to form stars. The peak column densities for the four objects in this work are on the low-to-mid end of the range (3.95×10^{20} cm^{-2} for AGC 229398 at the least, 5.89×10^{20} cm^{-2} for AGC 333576 at the most), so one could suggest that they did not have a high enough gas density for efficient star formation as an explanation for their high H I-to-optical-light ratios.

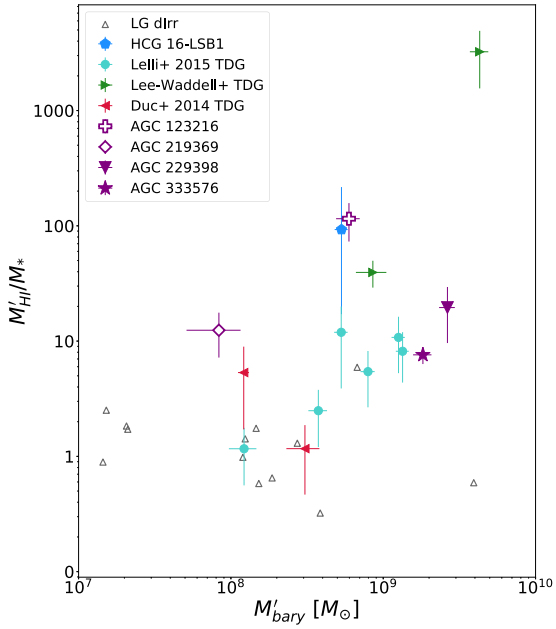

Figure 20. Comparison of H I-to-stellar mass vs. baryonic mass for objects from this work (purple, various symbols) to the young TDG candidate HCG 16-LSB1 (Román et al. 2021; blue pentagon), AD-TDG candidates from Lee-Waddell et al. (2016; green right-pointing triangles), TDG candidates from Lelli et al. (2015; turquoise circles), and likely older TDGs identified in McConnachie (2012; red left-pointing triangles). $M'_{\rm HI}$ and $M'_{\rm bary}$ for the objects from this work and from Lee-Waddell et al. (2016) are calculated with the ALFALFA measurements (Haynes et al. 2018). The H I masses for the Duc et al. (2014) TDGs used in the baryonic mass calculation are from Duc et al. (2011). For the comparison of TDG properties to those of normal (non-TDG) dwarf galaxies, we have plotted Local Group dIrrs from McConnachie (2012; dark gray triangles). As with Figure 19, filled symbols correspond to objects that have been identified as TDGs.

On the other hand, TDGs are expected to have a burst of star formation during their formation, due to the instability of the gas from turbulence, and then fade over time, which would also result in a higher H I-to-optical-light ratio as they age. For example, Román et al. (2021) predicted the evolution of the surface brightness for HCG 16-LSB1 based on its metallicity and the aging of its stellar population. They expect that the dimming of HCG 16-LSB1 will be rather extreme; in 400 Myr, the effective surface brightness will decrease by more than 1 mag arcsec^{-2}, making it fall below the optical threshold of the survey used in their work (DECaLS). Stellar populations with higher metallicities will experience more dimming, which means that TDGs will be particularly affected, though they are assumed to continue forming stars at a lower rate (Duc et al. 2014). This means that an evolved TDG could have a stellar population mainly formed in an initial burst followed by a lower rate of formation, but a high H I-to-optical-light ratio due to dimming.

While this idea does not easily distinguish TDGs from dIrr galaxies that have produced stars normally, objects that are faint due to a lack of stars proportional to their H I contents may be considered less likely to be TDGs because they likely did not have this initial burst of star formation. Figure 20, which plots the H I-to-stellar mass ratio against the baryonic mass of each object, demonstrates how this appears to be true for AGC 123216, which has an extreme $M'_{\rm HI}/M_*$ of 115.28 ± 42.20. This could mean that AGC 123216 lacked the star formation burst at its formation that would be expected for a TDG. HCG 16-LSB1 and AGC 208457 also fall higher than the distribution of the rest of the TDGs, even though they are confirmed tidal objects. Considering the young age of HCG 16-LSB1 ($57.9^{+21.7}_{-9.4}$ Myr according to Román et al. 2021) and the possible still-extant tidal tail and estimated age range of 6–2600 Myr for AGC 208457 (Lee-Waddell et al. 2016), they might have a high H I-to-stellar mass ratio because they are so young that they have not had sufficient time to convert gas into stars. The two older TDGs from Duc et al. (2014) have relatively average H I-to-stellar mass ratios compared to the TDGs from Lelli et al. (2015). Figure 20 also shows that the other three AD-TDG candidates appear to have $M'_{\rm HI}/M_*$, which is comparable to these TDGs and about an order of magnitude higher than dwarf irregulars. This suggests that their high H I-to-optical-light ratios may be the result of dimming rather than a deficit of stars in proportion to their H I content.

Due to this dimming, we can also expect TDGs to increasingly be found on the lower end of the central surface brightness versus stellar mass relationship as they age. Figure 21 shows that this is the case for the older TDGs from Duc et al. (2014), while younger TDGs (HCG 16-LSB1, the sample from Lelli et al. 2015), though still low, are more scattered along the relation shown by the comparative non-TDG sample, which is comprised of dwarf irregulars in the Local Group and dwarf ellipticals from the Hydra I cluster (Misgeld et al. 2008; Misgeld & Hilker 2011; McConnachie 2012). AGC 229398 and AGC 333576 also have low central surface brightnesses for their stellar masses, appearing quite similar to NGC 5557-E1. AGC 123216 and AGC 219369 are located within the distribution of dwarf ellipticals, so their central surface brightnesses are low compared to dwarf irregular galaxies of similar stellar mass. HCG 16-LSB1 is similarly placed, though it is unknown whether this is because it is so young that it simply may not have had enough time to form a larger stellar population yet. Over time, it is expected to eventually move farther right and lower in the plot as it forms stars and dims. It is important to note that though UDGs are not shown here, because they are defined as having $\mu_{g,0} > 24$ mag arcsec^{-2} (van Dokkum et al. 2015) they will also occupy the lower portion of the plot and may overlap with the evolved TDGs.

Duc et al. (2014) considered a comparison of the effective radius to the stellar mass as a tool for the optical identification of TDG candidates. TDGs tend to have effective radii larger than those of dwarf irregulars or dwarf ellipticals of a comparable stellar mass. In this sense, they resemble UDGs because their stellar mass is more spread out than usual. In the comparison of the effective radius to the stellar mass in Figure 22, it is clear that other identified TDGs occupy the top part of the distribution. AGC 229398 and AGC 333576 are located well above the distribution, along with the TDGs from Lee-Waddell et al. (2016). AGC 123216 and AGC 219369 appear to be on the upper end of the distribution as well (though not as dramatically as the other two objects).

5.5. Estimation of Travel Time

It is common to use the combination of stellar population models and photometry in multiple bands to estimate the age and metallicity of a galaxy (Bruzual & Charlot 2003). Our photometry in g and r bands for our TDG candidates is not sufficient to break the age–metallicity degeneracy associated with some broadband filter combinations, and a third filter (e.g., i band) would be required. Therefore, we must turn to

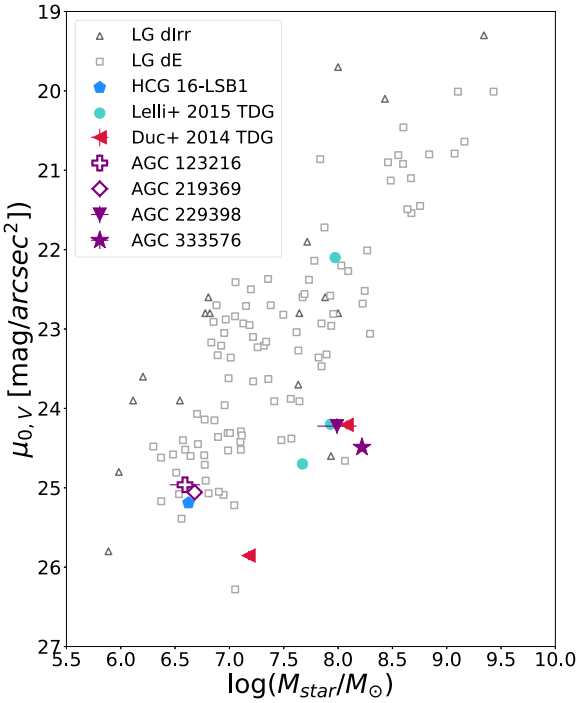

Figure 21. Comparison of central surface brightness vs. stellar mass for objects from this work (purple, various symbols) to the young TDG candidate HCG 16-LSB1 (Román et al. 2021; blue pentagon), TDG candidates discussed in Lelli et al. (2015; turquoise circles), and likely older TDGs identified in Duc et al. (2014; red left-pointing triangles). The non-TDG dwarf galaxy comparison samples plotted are Local Group dwarf irregulars from McConnachie (2012; dark gray triangles) and Hydra I cluster dwarf ellipticals whose properties were compiled by Misgeld et al. (2008) and Misgeld & Hilker (2011; light gray squares). Conversions from surface brightness in g to V were made with the Jester et al. (2005) transformation equations and the central color of the object where possible. If the central color was not known, the total $g - r$ color of the object was used, and if no color information was given, an average estimate of 0.4 ± 0.1 for dwarf galaxies based on the colors of Honey et al. (2018) was used. As with Figure 19, filled symbols correspond to objects that have been identified as TDGs.

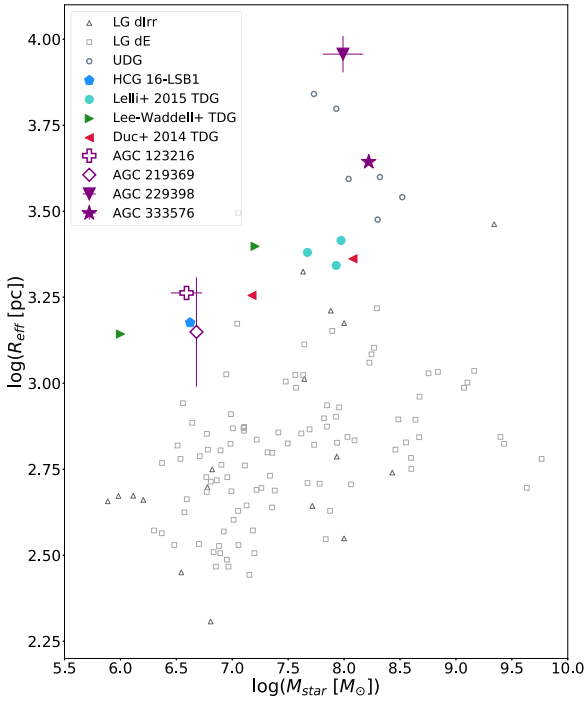

Figure 22. Comparison of effective radius vs. stellar mass for objects from this work (purple, various symbols) to the young TDG candidate HCG 16-LSB1 (Román et al. 2021; blue pentagon), AD-TDG candidates from Lee-Waddell et al. (2016; green right-pointing triangles), TDG candidates from Lelli et al. (2015; turquoise circles), and likely older TDGs identified in Duc et al. (2014; red left-pointing triangles). We have also plotted the sample of UDGs from Mancera Piña et al. (2020; dark gray circles). For the comparison of TDG properties to those of normal (non-TDG) dwarf galaxies, we have plotted Local Group dIrrs from McConnachie (2012; dark gray triangles), and Hydra I cluster dwarf ellipticals compiled by Misgeld & Hilker (20111; light gray squares). As with Figure 19, filled symbols correspond to objects that have been identified as TDGs.

other methods to evaluate the evolutionary histories of the sample galaxies.

The simulations from Bournaud & Duc (2006) give us a few markers to estimate the evolutionary progress of the TDG systems. They show that tidal tails fade within 300–500 Myr, so based on the absence of tidal tails, our TDG candidates would be at least a few hundred million years old if they are genuine TDGs. This alone would make them older than the majority of previously studied TDGs. TDGs face many obstacles to their survival: a significant number simply fall back onto their parent galaxy, or are torn apart by tidal disruption from the progenitor galaxy or by feedback from star formation. Bournaud & Duc (2006) found that only 25% of tidal knots more massive than 10^8 $M_\odot$ survive longer than 800 Myr, and that 45% of knots surviving at least 1 Gyr have masses exceeding 10^9 $M_\odot$. Note that "surviving" in this simulation meant remaining above the detection threshold of 10^8 $M_\odot$ within a diameter of 3 kpc or 3×10^8 $M_\odot$ within a diameter of 6 kpc, due to computational constraints. The tidal knots may undergo mass loss that puts them below this threshold while still appearing as distinct, intact knots that would continue to be classified as candidate TDGs in a higher-resolution simulation than that from Bournaud & Duc (2006).

If the ADs in this study are indeed TDGs, they are located much farther from their parents than the majority of previously proposed candidate TDGs, so it is necessary to show that it is possible for them to travel the observed distance in a reasonable timescale. The logic is similar to the logic we used to evaluate whether AGC 749170 could have reasonably reached its present location in 12 Myr, though now we consider rotational velocities and orientations of the potential parents. For each TDG–parent pair, we estimate a travel time as follows: TDGs are expected to have velocities with respect to their parent galaxies comparable to the rotational velocities of those parent galaxies (Bournaud & Duc 2006). We approximate the rotational velocity using

$$V'_{\rm rot} = \frac{W'_{20}}{2\sin(i)}, \tag{6}$$

with the W'_{20} value measured by the ALFALFA survey. Inclination i here is estimated from reported optical semimajor and semiminor axis measurements of the galaxy, using

$$\cos^2(i) = \frac{(b/a)^2 - q_0^2}{1 - q_0^2}, \tag{7}$$

with $q_0 = 0.13$ as is appropriate for spirals (all of the potential parent galaxies are classified as spirals with the exception of NGC 807, which nevertheless shows evidence of a disk). The resulting rotational velocities (and thus TDG candidate travel

velocities) are on the order of 100–300 km s^{-1}, which is typical for spiral galaxies and consistent with the velocities of the TDGs simulated by Bournaud & Duc (2006), so this is a reasonable estimate. TDGs in simulations tend to have low orbital inclination (<40°) with respect to the rotational plane of their progenitor (Bournaud & Duc 2006), so for simplicity we assume that the TDG candidate remained in the rotation plane of the parent. Therefore, we can use the inclination axis of the parent to deproject the angular separation on the sky and estimate a total travel distance for the TDG candidate. For this calculation, we consider the TDG candidates to be at the distance of the parent galaxy, give or take a negligible distance from any component of the velocity along the line-of-sight, which is consistent with the observations within uncertainties for all sources (given the previous assumption that AGC 219369 is at the distance of NGC 3510). With these approximations for the velocity and travel distance, we can estimate the time it would take for a newly formed TDG to travel to its current position from each potential parent. Ranges for the travel velocities, travel distance, and travel time estimates for each TDG–parent pair are included in Table 7. In most cases, it is reasonable for the candidate TDGs to travel the observed distance in several hundred megayears to a few gigayears. This timescale is also consistent with the absence of a tidal tail. The older TDGs identified in Duc et al. (2014) are estimated to be 2–4 Gyr, so our rough travel time estimates suggest that it is reasonable to think that our AD galaxies may indeed be older TDGs. Another way to evaluate whether these systems are in dynamical equilibrium would be to obtain resolved kinematics and compare the dynamical timescales with these travel times—if a dynamical time is much less than the estimated travel time, it becomes more likely that that system is dynamically stable.

Table 7
Estimated Travel Time for TDG–Parent Candidate Pairs

Source	Parent	Estimated Travel Velocity (km s^{-1})	Estimated Travel Distance (kpc)	Estimated Travel Time (Gyr)
AGC 123216	MRK 365	~210	260–310	1.2–1.4
	NGC 807	310–360	300–350	0.8–1.1
	MCG 05-06-003	100–110	900–1050	8.1–9.6
AGC 219369	NGC 3510	100–110	170–790	1.5–7.7
AGC 229398	KUG 1158+216	150–160	210–270	1.3–1.8
	UGC 6989	120–170	570–1020	3.2–8.2
AGC 333576	NGC 7775	140–220	150–170	0.7–1.2

5.6. The Origins of the Almost-Dark Galaxies in This Work

Much of the previous work on TDGs has been carried out with objects formed in merging galaxy systems, as ongoing interactions are easier to spot than past ones and the TDGs in these cases are readily identifiable as tidal debris. According to the simulations of Bournaud & Duc (2006), the interactions most likely to form long-lived TDGs are those that involve two gas-rich spiral galaxies with mass ratios of at least 1:8. Following the first pericenter passage of a gas-rich merging system, two opposing tidal tails of gas stretch out, and denser knots form along the tails relatively quickly. Knots located within the tails suffer significant mass loss and are more likely to fall back into the parent galaxies or disperse in under 1 Gyr, while those formed at the end (which also tend to be the most massive) have a better chance at long-term survival, becoming fully fledged TDGs (Bournaud & Duc 2006).

Another proposed formation mechanism for TDGs is a high-velocity encounter. Duc & Bournaud (2008) suggest that high-velocity encounters can produce independent H I clouds with minimal stellar content, resulting in tidal debris that is gas-rich but extremely optically faint. This scenario would explain the lack of a disrupting companion and the apparent minimal perturbation of the stellar disk for many of the proposed parents. Duc & Bournaud (2008) simulated the results of various encounters at ~300–1000 km s^{-1} and showed that flybys of 1000 km s^{-1} or more are capable of producing primary tidal tails that are just as long as those in merger scenarios. Rather than the two large tails produced in a standard major merger, the tidal tails formed in the high-velocity flyby consist of a long tail and a fainter, shorter countertail that quickly falls back onto the parent's disk. The tails have a lower stellar content than tails produced in a lower-velocity interaction (i.e., a galaxy merger) because most stars remain in the disk. While the total mass of gas removed from the parent in a high-velocity flyby is much lower than in a more traditional merger scenario, this is due to the shortness of the countertail; the gas mass of the primary tidal tail is comparable to the mass of an individual tail in a slower encounter. According to Duc & Bournaud (2008), the velocity of the tail is determined by the mass of the progenitor galaxy, not the speed of the interloper, and is on the same order of magnitude as the rotational velocity of the parent, so the reasoning behind the travel times as calculated in Section 5.5 should still be valid for TDGs formed in this way. With this understanding of how TDGs can form, we now move on to examining the potential origins of each system presented here.

AGC 123216 is the most ambiguous and complex case in the sample. AGC 123216 has three potential parents, two of which show signs of a previous interaction (the elongation of the H I around NGC 807, and the slight offset of H I from the optical center of MRK 365). The disturbance around NGC 807 is much more pronounced, and so it would be considered the primary candidate for providing most of AGC 123216's material. The estimated travel time for AGC 123216 from NGC 807 (assuming its relative travel speed is similar to NGC 807's rotation velocity) is around 1 Gyr. This is also approximately the timescale that Young (2002) estimates for the asymmetry of the CO gas to settle, though they note that the molecular gas may be farther from the center than it appears, which would extend this timescale. Young (2002) also mentions that the gas in this galaxy may have come from a merger between two gas-rich spiral galaxies, an event which potentially could have produced a TDG. If AGC 123216 is a TDG and was instead created by a later flyby interaction, MRK 365 is near the direction of travel that we would expect for an interloper, and would only need a velocity of ~600 km s^{-1} relative to NGC 807 to reach its current position in 1 Gyr. AGC 123216 has a large effective radius for its stellar mass, which would be expected for a TDG.

However, the dark matter content of AGC 123216 appears to be rather high for a TDG candidate. The object is well separated from the surrounding H I sources, so it is valid to assume that it is dynamically stable. Wang et al. (2020) studied other ADs with properties similar to AGC 123216 and found that they had low molecular-to-atomic gas mass ratios, so it seems unlikely that there is a large deposit of unseen molecular gas. Therefore, the majority of the unseen mass is likely to be nonbaryonic dark matter. It is important to remember that the results here represent an upper limit for the dynamical mass ratio, because the kinematic modeling indicated that the velocity dispersion was on the same order of magnitude as the rotation velocity and so the emission-line width would be artificially broadened (Lelli et al. 2015). This would mean the dynamical mass ratio (which is already somewhat low compared to most of the LG dwarf irregular galaxies) is potentially lower than we have estimated here (Figure 19). This makes it challenging to definitively say that AGC 123215 is not a TDG based solely on the estimate of the dark matter content. AGC 123216 also has an unusually high H I-to-stellar mass ratio compared to other TDGs, which could indicate it never experienced the increased rate of star formation expected to occur for TDGs when they form. AGC 123216 has many properties in common with the ALFALFA AD sources in the HI1232+20 system investigated by Janowiecki et al. (2015). That work concluded that AGC 229383, AGC 229384, and AGC 229385 were too isolated to be likely tidal features, and all three objects have some of the highest H I-to-stellar mass ratios measured to date for the AD sample (Janowiecki et al. 2015). If the objects in Janowiecki et al. (2015) are indeed nontidal, they could potentially be genuine "dark" galaxies–otherwise ordinary dwarf galaxies with unusually low stellar masses for the gaseous matter present. Janowiecki et al. (2015) also found that these objects appear to rotate slower than their measured baryonic mass would imply based on the baryonic Tully–Fisher relation (BTFR). The width of the velocity profile of AGC 123216 is rather small for a rotating disk of similar baryonic mass, and the velocity gradient map appears to show some minor ordered rotation (Figure 1b), which is supported by the kinematic model. AGC 123216's BTFR location, effective radius, and low surface brightness are also similar to those of UDGs (van Dokkum et al. 2015; Mancera Piña et al. 2019), though the distinction between a UDG and an "almost-dark" galaxy is not well defined.

AGC 219369 is possibly located very near to NGC 3510, which clearly has significant disruption to its H I distribution, so at first glance AGC 219369 is a good candidate to be a TDG. The edge-on orientation of NGC 3510 (Figure 11 and Figure 12) makes it difficult to evaluate the state of the stellar disk, but the stretched stellar limbs suggest that it has been severely disturbed. The orientation of NGC 3510 also makes it difficult to estimate the travel time for AGC 219369 (see the wide range in Table 7; additionally, if the angular separation is used as a minimum travel distance, it could be as low as 0.5 Gyr). The very blue color of NGC 3510 suggests that there has been fairly recent star formation activity, which may help constrain the length of time since the interaction. A more face-on orientation of NGC 3510 may have revealed a second interacting galaxy. NGC 3510 appears to be in a group with three other nearby galaxies (UGCA 225, UGC 6102, and NGC 3486), so a flyby scenario for the disruption of NGC 3510 (potentially resulting in the formation of AGC 219369) is also possible. However, the high dynamical mass ratio indicates AGC 219369 is more likely to be a dark matter dominated dwarf irregular galaxy. It is possible that AGC 219369 was a preexisting dwarf irregular galaxy which interacted with NGC 3510 in the past and caused the disruption of its H I, and not a post-interaction product such as a TDG. The large effective radius may be explained by the fact that preexisting dwarf galaxies may experience a temporary increase in size following tidal threshing, as shown in Paudel et al. (2013). On the other hand, it seems unlikely that an object as small as AGC 219369 could have caused such a large disturbance to the much more massive NGC 3510 and remained intact. We must also consider that AGC 219369 may be closer than 16.7 Mpc and the disturbed state of NGC 3510 may be entirely unrelated. If AGC 219369 is at a distance of 9.2 Mpc, the dynamical mass ratio would be even higher and the effective radius and stellar mass would be smaller. This means that the central surface brightness and effective radius would be closer to those of other dwarf irregular galaxies of similar stellar mass. For these reasons, we consider AGC 219369 unlikely to be a TDG. While the central surface brightness is fainter than 24 mag arcsec^{-2} , the effective radius is at most 1.41 ± 0.52 kpc, which is not large enough to clearly classify it as a UDG (van Dokkum et al. 2015). Therefore, we will simply identify AGC 219369 as a low-surface-brightness dwarf irregular galaxy.

AGC 229398 and AGC 333576 appear to have low dark matter contents (Figure 19), and very large effective radii for their stellar masses (Figure 22), both of which are indicators that they may be TDGs. They also have fainter central surface brightnesses compared to dwarf irregular and dwarf elliptical galaxies of similar stellar mass (Figure 21), which suggests their stellar populations may have dimmed over time, as is expected for TDGs. AGC 229398 has two potential parents identified by the velocity and angular separation selection criteria: KUG 1158+216 and UGC 6989. Based on mass ratio predictions for TDGs and their parents, AGC 229398 seems too massive to have come out of KUG 1158+216, so we turn our attention to UGC 6989. The mass ratio is still higher than that predicted by simulations, but more viable than for KUG 1158 +216. However, UGC 6989 is 482 kpc away from AGC 229398 on the sky, much farther than any other TDG–parent system studied. The TDGs simulated in Bournaud & Duc (2006) could have travel velocities ranging from 50 to 400 km s^{-1} relative to a parent with a virial velocity of 220 km s^{-1}, so we could consider the case of a TDG travel speed of 400 km s^{-1} and the minimum travel distance of 445 kpc (using the Haynes et al. (2018) distance of UGC 6989) to estimate a minimum travel time of 1.09 Gyr between UGC 6989 and the current location of AGC 229398. This would be an extreme case, so it is likely that AGC 229398 would be older than this; the travel times estimated in Table 7 are at least 3.2 Gyr. The $g - r$ color of AGC 229398 is 0.35, making it the reddest TDG candidate in our sample; this is consistent with it also being the oldest. UGC 6989's undisturbed spiral structure suggests that it is unlikely to have undergone a recent major merger, but a high-velocity flyby could have pulled off gas without disrupting the interior disk. There is no obvious interloper candidate in the images, but UGC 6989 was already at the limits of the selection criteria; whatever speed AGC 229398 is traveling at relative to UGC 6989, the interloper would only need to go a little more than twice that speed to end up outside

of the angular separation selection criteria and be overlooked. Duc & Bournaud (2008) notes that in 2 Gyr, an interloper traveling at 1000 km s^{-1} relative to the parent galaxy could be a projected distance of 2 Mpc away—at the distance of AGC 229398, this is over 1° of separation, outside the field of view of the pODI images.

AGC 333576 seems to have a more obvious progenitor: the nearby spiral galaxy NGC 7775. The H I gas surrounding NGC 7775 is distorted in the direction of AGC 333576, and the distorted stellar arms and bright region of star formation in the southwest imply a recent interaction of some kind. A major merger would likely have disrupted the structure of the arms even further, but a flyby interaction might not have, so we searched the field surrounding AGC 333576 and found the elliptical galaxy WISEA J235250.49+284555.2. As an elliptical galaxy, WISEA J235250.49+284555.2 would not have possessed very much gas and so would not have been the main contributor to a tidal dwarf, but it might have flown by NGC 7775 and pulled out the material from that disk, producing AGC 333576. The proximity of these galaxies implies that the interaction would not have happened a very long time ago, with travel time estimates for AGC 333576 from NGC 7775 between 0.7 and 1.2 Gyr; this is enough time for the majority of the gaseous tidal tail to have disappeared, but the end of a stellar tail connected to NGC 7775 is still slightly visible on the north side (Figure 18, left). Depending on the parameters of the interaction, the countertail may have been very short, which could explain why there is no strong evidence of one; the star formation region is located roughly opposite the stellar tail and might have been triggered by the same tidal forces.

6. Summary

We have investigated the H I and optical properties and possible origins of four Almost-Dark galaxies selected from the ALFALFA survey. After exploring H I kinematics and analyzing deep optical images, we concluded that AGC 229398 and AGC 333576 are the likeliest candidates to be TDGs based on their apparent low dark matter content and large effective radii compared to other dwarf irregular and elliptical galaxies of similar stellar masses. AGC 123216 is ambiguous—it is near other galaxies with large H I reservoirs that have clearly had an interaction of some kind, and it has a large effective radius. Its central surface brightness is also low compared to dwarf irregular galaxies of similar stellar mass. However, the upper limit on the dark matter content is too high to positively confirm it as a TDG, and it has an unusually high H I-to-stellar mass ratio for a TDG that should have formed stars when it was created. AGC 123216 also meets the criteria outlined in van Dokkum et al. (2015) for a UDG. AGC 219369 is most likely to be a low-surface-brightness dwarf irregular galaxy. While AGC 219369 appears in the sky near the spiral galaxy NGC 3510 (which has undergone some kind of interaction that disrupted its H I and stellar distributions), it appears to be dominated by dark matter and therefore is unlikely to have formed via the same tidal processes that create TDGs. All four objects would benefit from higher-resolution H I observations to better constrain their kinematics and dynamical masses.

In this study, we distinguished TDG candidates from irregular dwarf galaxies based on their low dark matter content and larger than expected effective radius for their stellar content. These candidate TDGs are located farther from any potential parents than the vast majority of previously studied TDGs, and the tidal tail from which they would have formed is nowhere to be found. While nearby surrounding galaxies often have disrupted H I distributions, none show clear signs of a recent merger that would be the expected source for a TDG. This suggests that either enough time has passed for the parent galaxy to mostly restabilize, or that the interaction was one that did not cause obvious disruption to the stellar disk. The overall picture provided by the H I and optical measurements of these objects suggests that they are older and more evolved than most of the TDGs that have previously been identified. Blind H I surveys with wide-field coverage like ALFALFA provide an opportunity to detect TDGs that have moved away from their parents and become optically fainter over their evolution, and which may be missed in more traditional optical surveys that prioritize stellar emission. Such surveys provide us with a more complete picture of galaxy formation and evolution at the low-mass end of the H I mass function.

The authors acknowledge the ALFALFA collaboration's work in observing, processing, and extracting sources. The authors would also like to thank the anonymous referee for their thorough comments, which greatly improved the quality of the manuscript.

L.M.G. acknowledges support from the Indiana Space Grant Consortium and thanks Laura Hunter for her explanations about the nuances of radio astronomy. This work was supported in part by NSF grant AST-1615483 to K.L.R. L.L. acknowledges support from NSF grant AST-2045369. M.P.H. acknowledges support from NSF/AST-1714828 and grants from the Brinson Foundation. E.A.K.A. is supported by the WISE research program, which is financed by the Dutch Research Council (NWO). J.M.C. and J.F. are supported by NSF grant AST-2009894. We thank the Indiana University (IU) College of Arts and Sciences for funding IU's share of the WIYN telescope.

We thank the staff of the WIYN Observatory and Kitt Peak National Observatory for their help and support during our WIYN pODI observing runs. We are grateful to the staff members at WIYN, NOIRLab, and Indiana University Pervasive Technology Institute for designing and implementing the ODI-PPA and assisting us with the pODI data reduction. We owe special thanks to Wilson Liu for helping us to troubleshoot and optimize the ODI image stacking process.

Funding for SDSS-III and SDSS-IV has been provided by the Alfred P. Sloan Foundation, the Participating Institutions, the National Science Foundation, and the U.S. Department of Energy Office of Science. SDSS acknowledges support and resources from the Center for High-Performance Computing at the University of Utah. The SDSS website is www.sdss.org.

Facilities: Arecibo, WIYN (pODI and ODI), WSRT.

Appendix
H I Channel Maps

Here we present the WSRT H i emission-line channel maps and the corresponding best-fitting kinematic models for AGC 123216 (Figure A1), AGC 219369 (Figure A2), AGC 229398 (Figure A3), and AGC 333576 (Figure A4). AGC 123216 and AGC 333576 show the clearest signs of rotation and have models that most closely resemble the data, followed by AGC 219369. The data for AGC 229398 do not demonstrate a clear

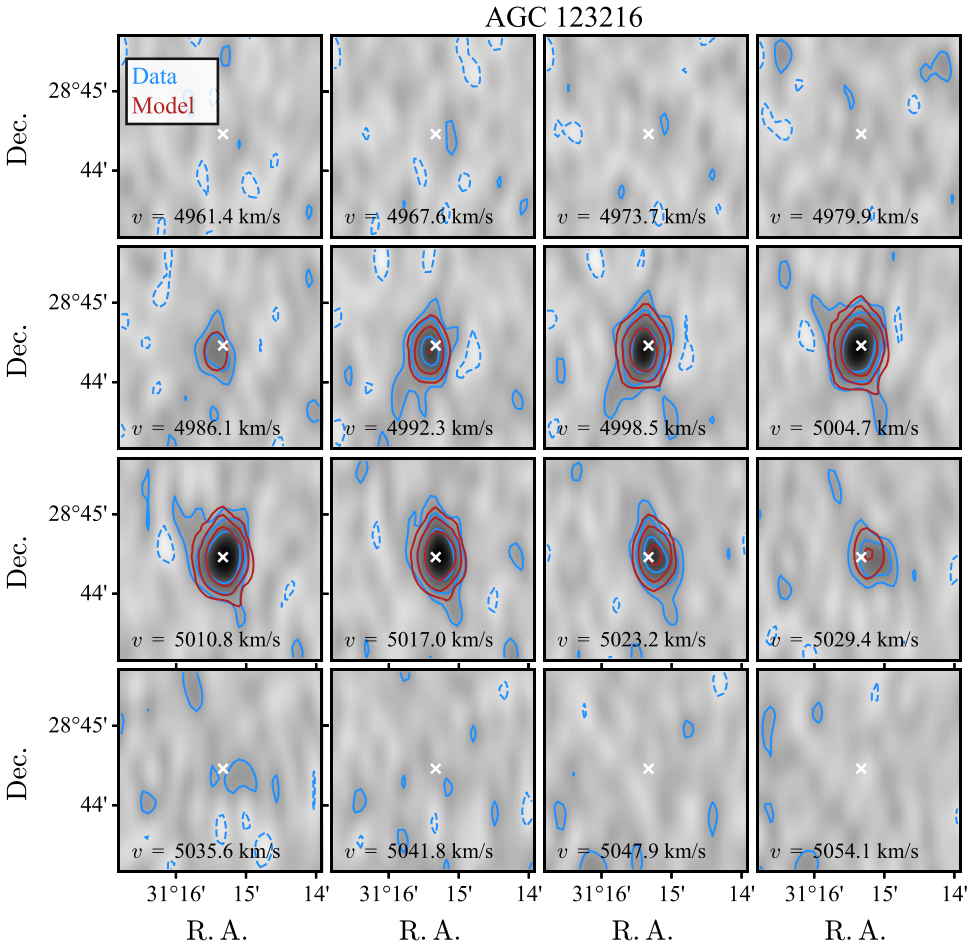

Figure A1. H I emission-line channel maps for AGC 123216 from WSRT data. The white cross marks the center of the galaxy and the velocity for each channel map is listed in the lower left corner. The emission of the galaxy is displayed by gray background and blue contour lines. The best-fitting model is shown by the red contour lines. Solid contours are at 2, 4, and 8 times the S/N of the data, and dashed contours represent $-2 \times$ S/N.

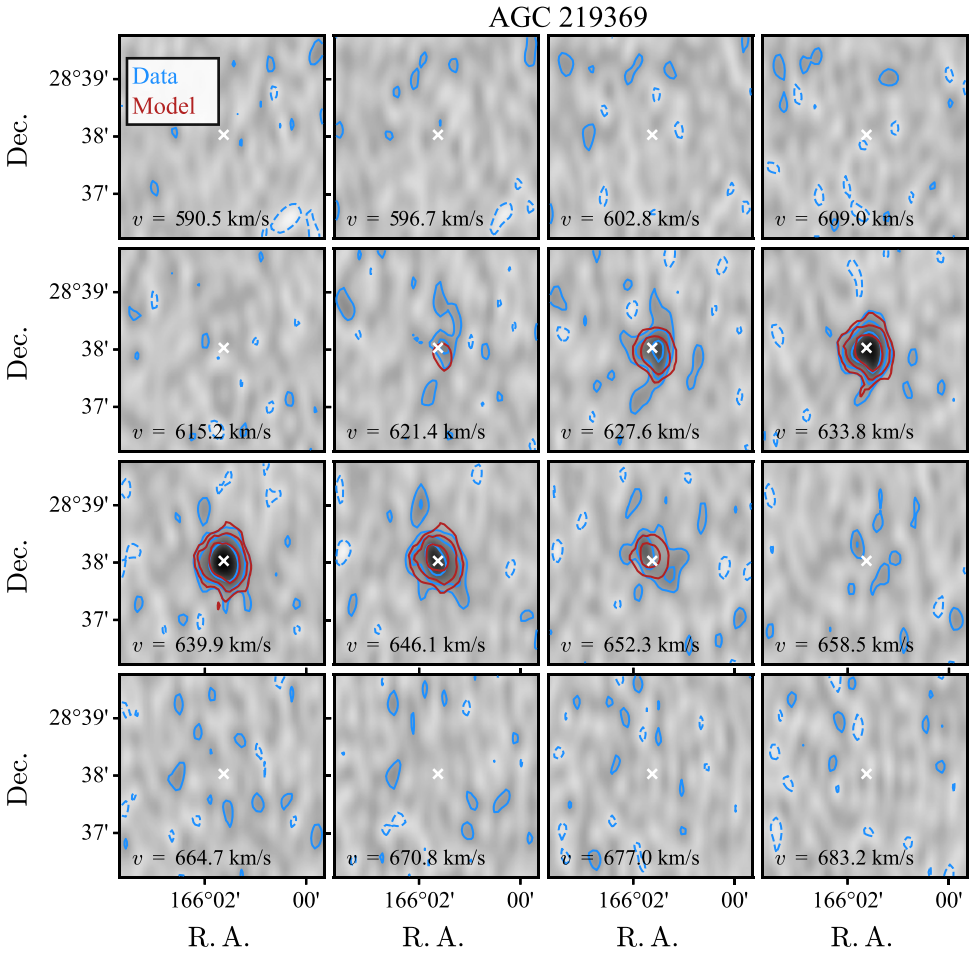

Figure A2. H I emission-line channel maps for AGC 219369 from WSRT data. The white cross marks the center of the galaxy and the velocity for each channel map is listed in the lower left corner. The emission of the galaxy is displayed by gray background and blue contour lines. The best-fitting model is shown by the red contour lines. Solid contours are at 2, 4, and 8 times the S/N of the data, and dashed contours represent $-2 \times$ S/N.

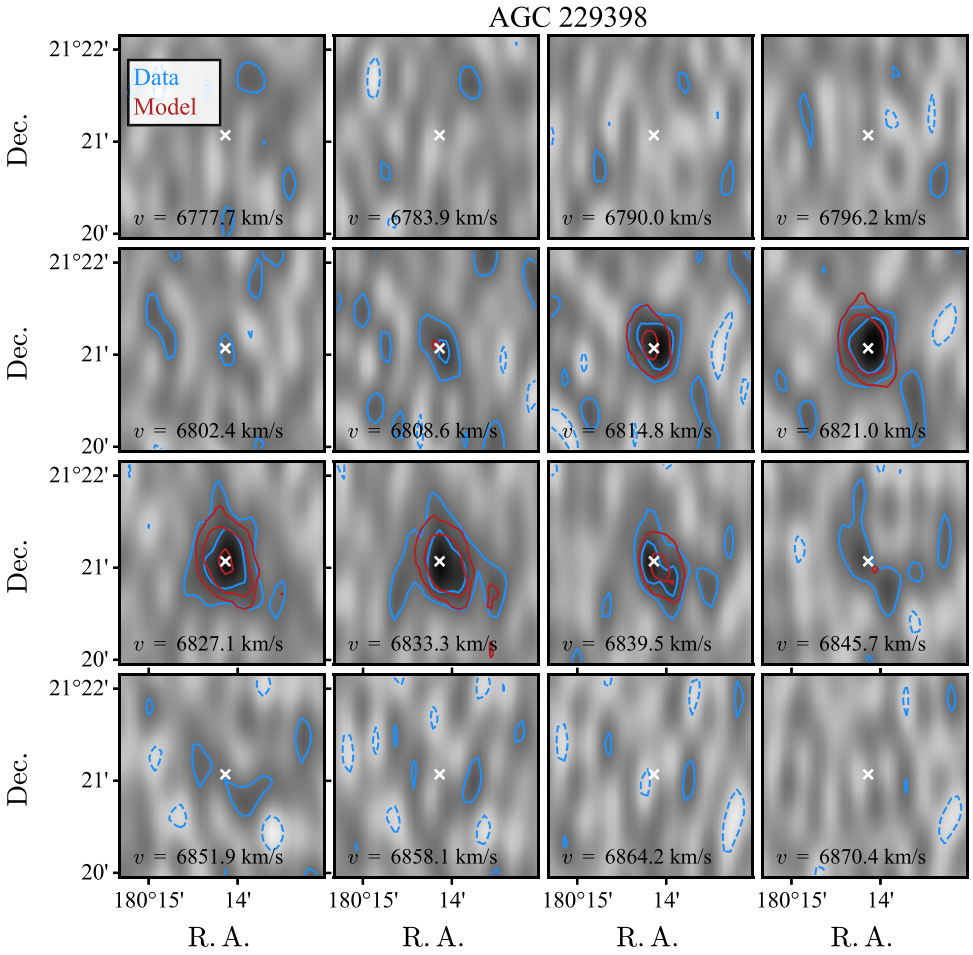

Figure A3. H I emission-line channel maps for AGC 229398 from WSRT data. The white cross marks the center of the galaxy and the velocity for each channel map is listed in the lower left corner. The emission of the galaxy is displayed by gray background and blue contour lines. The best-fitting model is shown by the red contour lines. Solid contours are at 2, 4, and 8 times the S/N of the data, and dashed contours represent $-2 \times$ S/N.

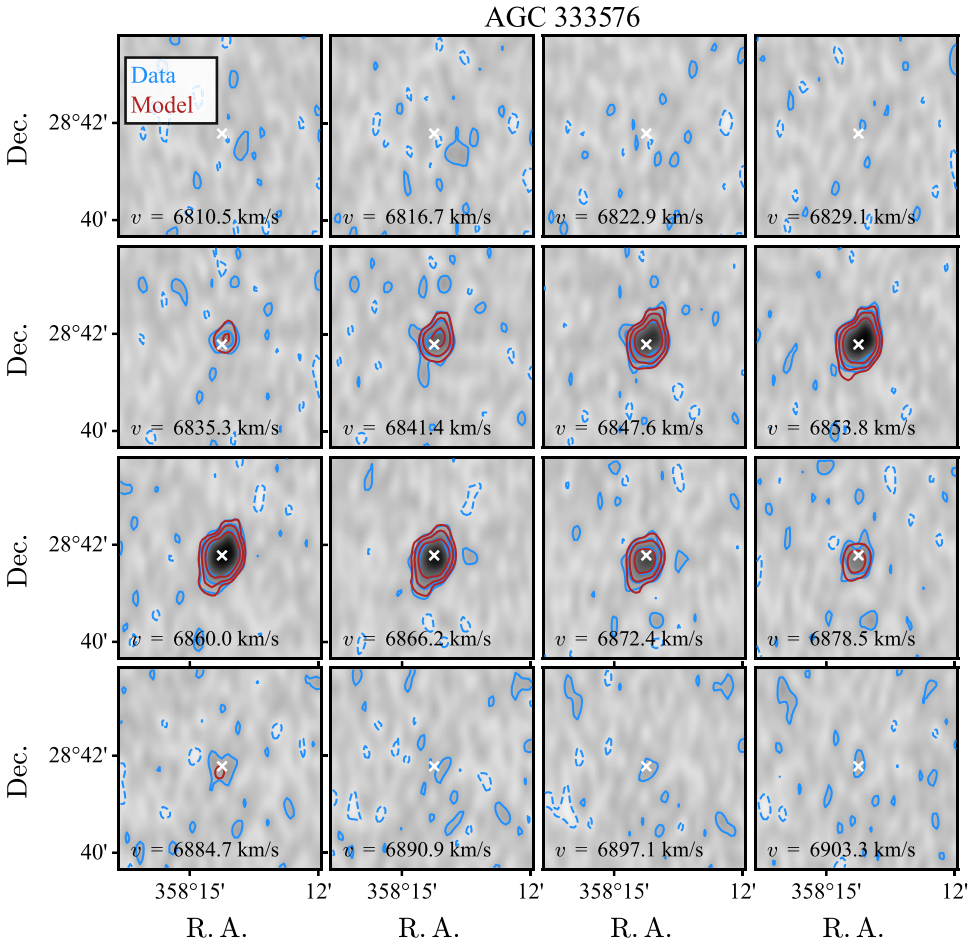

Figure A4. H I emission-line channel maps for AGC 333576 from WSRT data. The white cross marks the center of the galaxy and the velocity for each channel map is listed in the lower left corner. The emission of the galaxy is displayed by gray background and blue contour lines. The best-fitting model is shown by the red contour lines. Solid contours are at 2, 4, and 8 times the S/N of the data, and dashed contours represent $-2 \times$ S/N.

rotation gradient, and the model is a poor fit for the data, which indicates it may be more pressure supported than rotation supported.

ORCID iDs

Laurin M. Gray https://orcid.org/0000-0001-6389-5639
Katherine L. Rhode https://orcid.org/0000-0001-8283-4591
Lukas Leisman https://orcid.org/0000-0001-8849-7987
Pavel E. Mancera Piña https://orcid.org/0000-0001-5175-939X
John M. Cannon https://orcid.org/0000-0002-1821-7019
John J. Salzer https://orcid.org/0000-0001-8483-603X
Lexi Gault https://orcid.org/0000-0002-2492-7973
Jackson Fuson https://orcid.org/0000-0002-8598-439X
Gyula I. G. Józsa https://orcid.org/0000-0003-0608-6258
Elizabeth A. K. Adams https://orcid.org/0000-0002-9798-5111
Nicholas J. Smith https://orcid.org/0000-0002-3222-2949
Martha P. Haynes https://orcid.org/0000-0001-5334-5166
Steven Janowiecki https://orcid.org/0000-0001-9165-8905

References

Adams, E. A. K., Giovanelli, R., & Haynes, M. P. 2013, ApJ, 768, 77
Ahumada, R., Prieto, C. A., Almeida, A., et al. 2020, ApJS, 249, 3
Albareti, F. D., Allende Prieto, C., Almeida, A., et al. 2017, ApJS, 233, 25
Bacchini, C., Fraternali, F., Pezzulli, G., & Marasco, A. 2020, A&A, 644, A125
Bertin, E., Mellier, Y., Radovich, M., et al. 2002, in ASP Conf. Ser. 281, Astronomical Data Analysis Software and Systems XI, ed. D. A. Bohlender, D. Durand, & T. H. Handley (San Francisco, CA: ASP), 228
Bournaud, F. 2010, AdAst, 2010, 735284
Bournaud, F., & Duc, P. A. 2006, A&A, 456, 481
Bournaud, F., Duc, P.-A., Brinks, E., et al. 2007, Sci, 316, 1166
Bruzual, G., & Charlot, S. 2003, MNRAS, 344, 1000
Cairós, L. M., Caon, N., Vílchez, J. M., González-Pérez, J. N., & Muñoz-Tuñón, C. 2001, ApJS, 136, 393
Cannon, J. M., Martinkus, C. P., Leisman, L., et al. 2015, AJ, 149, 72
Ciotti, L., & Bertin, G. 1999, A&A, 352, 447
Darg, D. W., Kaviraj, S., Lintott, C. J., et al. 2010, MNRAS, 401, 1043
de Blok, W. J. G., van der Hulst, J. M., & Bothun, G. D. 1995, MNRAS, 274, 235
de Vaucouleurs, G., de Vaucouleurs, A., Corwin, H. G. J., et al. 1991, Third Reference Catalogue of Bright Galaxies (New York: Springer-Verlag)
Di Teodoro, E. M., & Fraternali, F. 2015, MNRAS, 451, 3021
Dressel, L. L. 1987, in IAU Symp. 127, Structure and Dynamics of Elliptical Galaxies, ed. P. T. de Zeeuw (Dordrecht: Springer), 423
Du, W., Cheng, C., Zheng, Z., & Wu, H. 2020, AJ, 159, 138
Duc, P.-A., & Mirabel, I. F. 1999, in IAU Symp. 186, Galaxy Interactions at Low and High Redshift, ed. J. E. Barnes & D. B. Sanders (Cambridge: Cambridge Univ. Press), 61
Duc, P.-A. 2012, in ASSP 28, Dwarf Galaxies: Keys to Galaxy Formation and Evolution (Berlin: Springer), 305
Duc, P.-A., & Bournaud, F. 2008, ApJ, 673, 787
Duc, P. A., Braine, J., Lisenfeld, U., Brinks, E., & Boquien, M. 2007, A&A, 475, 187

Duc, P. A., Brinks, E., Springel, V., et al. 2000, AJ, 120, 1238
Duc, P.-A., Cuillandre, J.-C., Serra, P., et al. 2011, MNRAS, 417, 863
Duc, P.-A., Paudel, S., McDermid, R. M., et al. 2014, MNRAS, 440, 1458
Durbala, A., Finn, R. A., Crone Odekon, M., et al. 2020, AJ, 160, 271
Eisenstein, D. J., Weinberg, D. H., Agol, E., et al. 2011, AJ, 142, 72
Fixsen, D. J., Cheng, E. S., Gales, J. M., et al. 1996, ApJ, 473, 576
Fraternali, F., Karim, A., Magnelli, B., et al. 2021, A&A, 647, A194
Gault, L., Leisman, L., Adams, E. A. K., et al. 2021, ApJ, 909, 19
Gimeno, G. N., Díaz, R. J., & Carranza, G. J. 2004, AJ, 128, 62
Giovanelli, R., Haynes, M. P., Kent, B. R., et al. 2005, AJ, 130, 2598
Giovanelli, R., Haynes, M. P., Kent, B. R., & Adams, E. A. K. 2010, ApJL, 708, L22
Gopu, A., Hayashi, S., Young, M. D., et al. 2014, Proc. SPIE, 9152, 91520E
Hagen, L. M. Z., Seibert, M., Hagen, A., et al. 2016, ApJ, 826, 210
Harbeck, D. R., Boroson, T., Lesser, M., et al. 2014, Proc. SPIE, 9147, 91470P
Haynes, M. P., Giovanelli, R., Kent, B. R., et al. 2018, ApJ, 861, 49
Haynes, M. P., Giovanelli, R., Martin, A. M., et al. 2011, AJ, 142, 170
Herrmann, K. A., Hunter, D. A., Zhang, H.-X., & Elmegreen, B. G. 2016, AJ, 152, 177
Hibbard, J. E., van der Hulst, J. M., Barnes, J. E., & Rich, R. M. 2001, AJ, 122, 2969
Honey, M., van Driel, W., Das, M., & Martin, J. M. 2018, MNRAS, 476, 4488
Huchra, J. P., Macri, L. M., Masters, K. L., et al. 2012, ApJS, 199, 26
Hunter, D. A., Hunsberger, S. D., & Roye, E. W. 2000, ApJ, 542, 137
Iorio, G., Fraternali, F., Nipoti, C., et al. 2017, MNRAS, 466, 4159
Janesh, W., Rhode, K. L., Salzer, J. J., et al. 2019, AJ, 157, 183
Janowiecki, S., Leisman, L., Józsa, G., et al. 2015, ApJ, 801, 96
Jester, S., Schneider, D. P., Richards, G. T., et al. 2005, AJ, 130, 873
Józsa, G. I. G., Kenn, F., Klein, U., & Oosterloo, T. A. 2007, A&A, 468, 731
Kaviraj, S., Darg, D., Lintott, C., Schawinski, K., & Silk, J. 2012, MNRAS, 419, 70
Kotulla, R. 2014, in ASP Conf. Ser. 485, Astronomical Data Analysis Software and Systems XXIII, ed. N. Manset & P. Forshay (San Francisco, CA: ASP), 375
Kourkchi, E., Tully, R. B., Eftekharzadeh, S., et al. 2020, ApJ, 902, 145
Lang, Dustin 2014, AJ, 147, 108
Lee-Waddell, K., Madrid, J. P., Spekkens, K., et al. 2018, MNRAS, 480, 2719
Lee-Waddell, K., Spekkens, K., Chandra, P., et al. 2016, MNRAS, 460, 2945
Lee-Waddell, K., Spekkens, K., Cuillandre, J.-C., et al. 2014, MNRAS, 443, 3601
Lee-Waddell, K., Spekkens, K., Haynes, M. P., et al. 2012, MNRAS, 427, 2314
Leisman, L., Haynes, M. P., Giovanelli, R., et al. 2016, MNRAS, 463, 1692
Leisman, L., Haynes, M. P., Janowiecki, S., et al. 2017, ApJ, 842, 133
Leisman, L., Rhode, K. L., Ball, C., et al. 2021, AJ, 162, 274
Lelli, F., Duc, P.-A., Brinks, E., et al. 2015, A&A, 584, A113
Lucero, D. M., & Young, L. M. 2013, AJ, 145, 56
Mancera Piña, P. E., Fraternali, F., Adams, E. A. K., et al. 2019, ApJL, 883, L33
Mancera Piña, P. E., Fraternali, F., Oman, K. A., et al. 2020, MNRAS, 495, 3636
Mancera Piña, P. E., Fraternali, F., Oosterloo, T., et al. 2022a, MNRAS, 514, 3329
Mancera Piña, P. E., Fraternali, F., Oosterloo, T., et al. 2022b, MNRAS, 512, 3230
Marasco, A., Fraternali, F., Posti, L., et al. 2019, A&A, 621, L6
Marinoni, C., Monaco, P., Giuricin, G., & Costantini, B. 1998, ApJ, 505, 484
Masters, K. L. 2005, PhD thesis, Cornell Univ.
Mateo, M. L. 1998, ARA&A, 36, 435
McConnachie, A. W. 2012, AJ, 144, 4
McGaugh, S. S. 1992, PhD thesis, Univ. Michigan
Mezcua, M., Lobanov, A. P., Mediavilla, E., & Karouzos, M. 2014, ApJ, 784, 16
Misgeld, I., & Hilker, M. 2011, MNRAS, 414, 3699
Misgeld, I., Mieske, S., & Hilker, M. 2008, A&A, 486, 697
NASA/IPAC Extragalactic Database (NED) 2019, NASA/IPAC Extragalactic Database (NED), IPAC, doi:10.26132/NED1
Nilson, P. 1973, Uppsala General Catalogue Of Galaxies (Uppsala: Uppsala Astron. Obs.)
Paudel, S., Duc, P.-A., Côté, P., et al. 2013, ApJ, 767, 133
Rhode, K. L., Salzer, J. J., Haurberg, N. C., et al. 2013, AJ, 145, 149
Román, J., Jones, M. G., Montes, M., et al. 2021, A&A, 649, L14
Saintonge, A. 2007, AJ, 133, 2087
Salim, S., Boquien, M., & Lee, J. C. 2018, ApJ, 859, 11
Salim, S., Lee, J. C., Janowiecki, S., et al. 2016, ApJS, 227, 2
Sand, D. J., Crnojević, D., Bennet, P., et al. 2015, ApJ, 806, 95
Sault, R. J., Teuben, P. J., & Wright, M. C. H. 1995, in ASP Conf. Ser. 77, Astronomical Data Analysis Software and Systems IV, ed. R. A. Shaw, H. E. Payne, & J. J. E. Hayes (San Francisco, CA: ASP), 433
Schaye, J. 2004, ApJ, 609, 667
Schlafly, E. F., & Finkbeiner, D. P. 2011, ApJ, 737, 103
Schlegel, D. J., Finkbeiner, D. P., & Davis, M. 1998, ApJ, 500, 525
Sellwood, J. A., & Sanders, R. H. 2022, MNRAS, 514, 4008
Serra, P., Oosterloo, T., Morganti, R., et al. 2012, MNRAS, 422, 1835
Shaya, E. J., Tully, R. B., Hoffman, Y., & Pomarède, D. 2017, ApJ, 850, 207
Springob, C. M., Haynes, M. P., Giovanelli, R., & Kent, B. R. 2005, ApJS, 160, 149
Swaters, R. A. 1999, PhD thesis, Univ. Groningen
Theureau, G., Hanski, M. O., Coudreau, N., Hallet, N., & Martin, J. M. 2007, A&A, 465, 71
Thuan, T. X., Lipovetsky, V. A., Martin, J. M., & Pustilnik, S. A. 1999, A&AS, 139, 1
Tully, R. B., Courtois, H. M., & Sorce, J. G. 2016, AJ, 152, 50
van Dokkum, P. G., Abraham, R., Merritt, A., et al. 2015, ApJL, 798, L45
Vorontsov-Vel'Yaminov, B. A., & Arkhipova, V. P. 1964, MCG, Part 2
Wang, J., Kauffmann, G., Józsa, G. I. G., et al. 2013, MNRAS, 433, 270
Wang, J., Yang, K., Zhang, Z.-Y., et al. 2020, MNRAS, 499, L26
Weilbacher, P. M., Duc, P. A., Fritze v. Alvensleben, U., Martin, P., & Fricke, K. J. 2000, A&A, 358, 819
Willmer, C. N. A. 2018, ApJS, 236, 47
Wright, Edward L., Eisenhardt, Peter R. M., Mainzer, Amy K., et al. 2010, AJ, 140, 1868
Young, J. S., & Scoville, N. Z. 1991, ARA&A, 29, 581
Young, L. M. 2002, AJ, 124, 788